FINAL

NASA/CR· -*1998* - 207479

IN -91-CR
063267

Continuing Studies of Planetary Atmospheres

Associated With Experiments

on the Galileo Jupiter Probe

and Infrared Observations of Venus

NASA-Ames Research Center
Cooperative Agreement
NCC 2-466

Status Report
Covering the Period of
January, 1998 through January, 1998

and

Final Report

Jindra Goodman, Project Director
Boris Ragent, Principal Investigator

San Jose State University Foundation
P.O. Box 720130
San Jose, California, 95172-0130

Summary of Research Activities During the Period of January, 1997 through January, 1998
and
Final Report on NASA-Ames Research Center Cooperative Agreement NCC 2-466

This report is the last Status Report and also the Final Report under NASA-Ames Cooperative Agreement NCC 2-466. The primary activities during this period involved (a) the continuing analyses of the results obtained from the Galileo Jupiter Mission Probe Nephelometer Experiment, the submission of these results for publication in a special issue of the Journal of Geophysical Research, revising and resubmission of this draft based upon the comments of peer reviewers and colleagues, and (b) the additional preparation of the results of some of the previous work performed under this agreement on the Venus atmosphere and clouds for further publication. These latter publications are expected to be submitted in the near future.

The final draft on the Jupiter work, to be published in the Journal of Geophysical Research, is appended as the major portion of this final report.

The Clouds of Jupiter:

Results of the Galileo Jupiter Mission Probe

Nephelometer Experiment

by

Boris Ragent and David S. Colburn

San Jose State University Foundation, 1 Washington Square, San Jose, California 95192

Kathy A. Rages

Space Physics Research Institute, 572 Hyannis Drive, Sunnyvale, California 94087

Tony C.D. Knight

2370 South Brentwood Street, Lakewood, Colorado 80227

Philip Avrin

Aerospace Corporation, 1150 Academy Parkway, Colorado Springs, Colorado 80912

Glenn S. Orton and Padmavati A. Yanamandra-Fisher

Jet Propulsion Laboratory, California Institute of Technology, 4800 Oak Grove Drive,

Pasadena, California 91109

and

Gerald W. Grams

Clark-Atlanta University, 223 James P. Brawley Drive, Atlanta, Georgia 30314

Abstract. The results of the nephelometer experiment conducted aboard the Probe of the Galileo mission to Jupiter are presented. The tenuous clouds and sparse particulate matter in the relatively particle-free 5-μm "hot spot" region of the Probe's descent were documented from about 0.46 bars to about 12 bars. Three regions of apparent coherent structure were noted, in addition to many indications of extremely small particle concentrations along the descent path . From the first valid measurement at about 0.46 bars down to about 0.55 bars a feeble decaying lower portion of a cloud, corresponding with the predicted ammonia particle cloud, was encountered. A denser, but still very modest, particle structure was present in the pressure regime extending from about 0.76 to a distinctive base at 1.34 bars, and is compatible with the expected ammonium hydrosulfide cloud. No massive water cloud was encountered, although below the second structure, a small, vertically thin layer at about 1.65 bars may be detached from the cloud above, but may also be water condensation, compatible with reported measurements of water abundance from other Galileo Mission experiments. A third small signal region, extending from about 1.9 to 4.5 bars, exhibited quite weak but still distinctive structure, and, although the identification of the light scatterers in this region is uncertain, may also be a water cloud perhaps associated with lateral atmospheric motion and/or reduced to a small mass density by atmospheric subsidence or other explanations. Rough descriptions of the particle size distributions and cloud properties in these regions have been derived, although they may be imprecise because of the small signals and experimental difficulties. These descriptions document the small number densities of particles, the moderate particle sizes, generally in the slightly submicron to few micron range, and the resulting small optical depths, mass densities due to particles, column particle number loading and column mass loading in the atmosphere encountered by the Galileo Probe during its descent.

1.0 Introduction

One of the principal objectives of the Galileo Mission to Jupiter was to determine the locations, horizontal and vertical extent, micro physical properties, and composition of the clouds of Jupiter. A nephelometer instrument (NEP) measuring light scattering from the ambient atmosphere at five scattering angles was included as part of the experiments package on the Galileo Mission Probe that entered the Jovian atmosphere on December 7, 1995. The purpose of this experiment was to establish the vertical location and to attempt to document the microphysical properties of the clouds along the Probe descent trajectory. It was hoped that the data would yield values of parameters required for radiation modeling studies, such as, for example, cloud particle size distributions, opacities, scattering and extinction cross sections, local total mass densities, etc., and that finding the location of the cloud physical boundaries would supplement other experimental data in helping to identify the chemical composition of the particles of the clouds and atmospheric species abundances. In addition, it was anticipated that the data obtained would furnish "ground truth" for the remote sensing observations to be conducted by the Galileo Mission Orbiter experiments.

The Galileo Probe entered the atmosphere of Jupiter at a latitude of about +5.9°, inside and near the southern edge of a so-called 5-μm "hot spot" [Orton et al., 1996], a region characterized by enhanced emission of 5 μm radiation emerging from deep in the atmosphere, which implies a region of reduced radiation-absorbing atmospheric component species and particle interaction. The first valid measurements obtained by the nephelometer occurred about 17.1 seconds after the instrument was turned on following Probe atmospheric entry. This time, about 3.5 seconds following parachute deployment and heat shield separation, and about 1.7 seconds following the deployment of the nephelometer mirror arm, corresponded to an ambient atmospheric pressure of 0.46 bars.

General descriptions of the Jovian clouds, based on assumptions of species abundances in the Jovian atmosphere and equilibrium thermochemistry, have been attempted, for

example, by *Weidenschilling and Lewis* [1973], *Atreya and Romani* [1985] and *Atreya* [1986]. Data on the cloud properties of Jupiter have also been obtained from many earth-based measurements (see the review by *West et al.*, 1986), earth-orbiting telescopes (*Chanover et al.*, 1997), and from interplanetary flyby missions (e.g. *Smith and Tomasko*, 1984). Summaries of our state of knowledge and uncertainties about the clouds have been published by a number of investigators such as *West et al.* [1986] and *Carlson et al.* [1988] and interpretations of the results of cloud measurements by *Bjoraker* [1985], *Carlson et al.* [1993], *Del Genio et al.* [1990], *Marten et al.* [1981], *Magalhaes et al.* [1990] and *Gierasch et al.* [1986].

Shortly after the Probe entry, supporting earth-based imaging reported that the Probe had entered a 5-μm "hot spot" [*Orton et al.*, 1996]. These regions are characterized by the emergence of thermal radiation from deep, warm levels of the atmosphere as a result of the absence of the cloud cover existing elsewhere on the planet. There are few descriptions of cloud structure specific to 5-μm hot spots in the literature prior to the Galileo mission. Much of what is available was covered in the extensive review of Jupiter's cloud properties by *West et al.* [1986]. Characterizations of 5-μm hot spots based on analysis of Jupiter's thermal spectrum shows a minimum of cloud opacity near or above the 600-mbar level where NH_3 gas should condense, based on Jupiter's spectrum in the atmospheric windows near 8.6 and 45 μm, where there is little sensitivity to particles deeper than the 1-bar level. *Marten et al.* [1981], and *Bézard et al.* [1983] argued that the low opacity of these spectral regions in Voyager IRIS spectra, combined with the need for some opacity in the 5-μm region, required some cloud opacity near the 2-bar level but not at the NH_3 cloud level. *Carlson et al.* [1993] performed a detailed analysis of Voyager IRIS spectra in hot spots (their "Category 8" spectra), also choosing very little optical thickness attributed to the NH_3 cloud ($\tau = 0.27 \pm 0.03$). However, the *Carlson, Lacis and Rossow* [1993] model for a ~2 bar cloud attributed to NH_4SH, yielded optical depths which were also low ($\tau = 0.02$, +0.08, -0.02) and contained a deeper-level H_2O cloud whose bottom was placed at 4.9 bars

and that assumed most of the cloud opacity of the region ($\tau = 4.0 \pm 1.0$). In addition, the thermal infrared spectra also argue against small particles dominating Jupiter's NH_3 cloud opacity, because no resonant absorption features of NH_3 ice are apparent in the Voyager IRIS spectra although other explanations for this effect have been proposed [*Clapp and Miller*, 1993]. A significant particle population with radii near 100 μm is preferred by *Marten et al.* [1981], and *Orton et al.* [1982], and near 3 - 100 μm by *Carlson , Lacis and Rossow* [1993]. A comparison of 5- and 45-μm radiances by *Gierasch, Conrath and Magalhaes* [1986] is consistent with modulation by NH_3 cloud particles in the 3-μm to 10-μm range.

However, from pre-Galileo observations in the wavelength range below 1 μm, a different characterization emerges. *Smith and Tomasko* [1984] showed that regions free of clouds down to the 2-bar level would produce observable polarization signatures in the Pioneer Imaging Photopolarimeter (IPP) data, but no such signatures are seen at hot spot latitudes. *West, Kupferman and Hart* [1985] compared opacities at 0.619 and 5 μm, including considerations of the weak CH_4 absorption. Both wavelengths are sensitive to radiation emerging from below the 5-bar level in the absence of particulate scattering or absorption. However, while 5-μm intensity increases dramatically over the two hot spots they examined, there are no observable enhancements in the equivalent width of the 0.619-μm CH_4 band. They suggest that the optical depth of particles at or above the 2-bar level is about 8 at 0.619 μm and a factor of 5 smaller at 5 μm, consistent with particles having an effective radius of about 1 μm. The Pioneer IPP polarization data suggest that at least 25% of the total cloud opacity is found between the ~600-mbar base of the NH_3 cloud and the 300-mbar level. *West, Kupferman and Hart* [1985] showed that a cloud of 1-μm particles in the NH_3 condensation region can account for the limb darkening seen at 5 μm in Voyager IRIS spectra, although the details of scattering by nonspherical NH_3 ice crystals would actually exert a strong influence on the limb darkening.

West, Strobel and Tomasko [1986] attempted to bring the eclectic set of observations and cloud models in the extant literature up to that time together into a single coherent picture which would address spatial inhomogeneities, among which were 5-μm hot spots. In their summary, a fairly ubiquitous haze layer lies at the top of the troposphere. The particles in this layer have an effective radius of 1 μm or less and a total optical thickness between 3 and 5. The top of this layer is at the 200-mbar pressure level, and the bottom is presumed to coincide with the ~600-mbar base of a condensate cloud of NH_3 ice. Because NH_3 ice is colorless, the ice particles must be mixed with an unknown constituent which provides the visible color of the clouds. Together with this stable layer of particles, lies a layer of 3 to 100-μm particles near the base of the NH_3 ice cloud. These particles are required to account for Jupiter's opacity at 45 μm and, we would add, at 8.57 μm, two windows longward of 5 μm in Jupiter's spectrum. These particles are at least partially responsible for modulating Jupiter's 5-μm radiance (*Orton and Terrile*, 1978; *Gierasch, Conrath and Magalhaes*, 1986), and, from data available prior to this mission, they are probably absent in the 5-μm hot spots.

West, Strobel and Tomasko [1986], felt that the bulk of evidence favored the existence of an inhomogeneous cloud at the 2-bar level. It would best account for the 5-μm spectrum, modulation of 5-μm radiances, and variations in the equivalent widths of CH_4, H_2O and NH_3 lines observed in reflected sunlight. From analysis of reflected sunlight, this cloud layer was often modeled merely as a semi-infinite cloud top with only the single-scattering albedo constrained by observations. Even with longer-wavelength observations, constraints on the vertical location of such a cloud were weak and constraints on the particle size nonexistent. Its composition was assumed to be solid NH_4SH particles, mixed with some chromophore constituent. This was based on thermochemical models (see, for example, *Weidenschilling and Lewis*, 1973; *Atreya and Romani*, 1985; *Lewis and Prinn*, 1984) as well as the need for particles darker than NH_4SH or H_2O. On the other hand, this cloud might be a condensate of H_2O if the oxygen abundance were 100 times less than

expected for a solar composition (*Bjoraker*, 1985). However, for a solar-like oxygen abundance, H_2O would condense around 6 bars. Few models place observable constraints on such a cloud other than *Carlson, Lacis and Rossow* [1993], although their model differs substantially from others by placing most of the 5-μm atmospheric opacity near the H_2O cloud, as noted earlier. While including the possibility of such an H_2O cloud, and mentioning that there may be some evidence to doubt its existence, *West, Strobel and Tomasko* [1986] note that such a cloud, as well as all other clouds, may be patchy, and may not be appreciably present in the hot spot region. Thus, *West, Strobel and Tomasko* [1986], interpreted the observable spatial modulations of radiance in 5-μm hot spots as variations of the properties of a 2-bar level cloud, accompanied by variations of the large-particle component of the NH_3 condensate layer cloud. *Bézard, Baluteau and Marten* [1983], in fact, interpreted the correlation of Voyager IRIS 5-μm and 45-μm radiation as a correlation of cloudiness at levels near 2 bars and in the NH_3 ice cloud. This is quite reasonable if vertical motions are correlated over the 600-mbar and the 2-bar levels.

More recently, another set of observations have been made of 5-μm hot spots from earth-based facilities in support of the Galileo Probe mission. The best spatial resolution from earth-based measurements has been from the Hubble Space Telescope Wide-Field / Planetary Camera-2 (WF/PC2) instrument. *Chanover, Kuehn and Beebe* [submitted to *Icarus*], and *Chanover* [1997] characterized properties of a 2-cloud model, constrained by WF/PC2 images of the center-to-limb behavior of dark areas near 6.5° N latitude which have been identified as regions of high 5-μm radiance (*Orton et al.*, 1996). The constraining data consisted of images taken on 1995 Feb 13 and 17, and on 1995 Oct 4, using a "continuum" filter with an effective wavelength of $\lambda = 0.9546$ μm ($\Delta\lambda = 0.0053$ μm) and a CH_4 absorption filter with $\lambda = 0.8929$ μm ($\Delta\lambda = 0.0064$ μm). They derived a stratospheric haze layer with visible optical thickness of 0.34, under which lay an NH_3 cloud deck whose top reaches ~200mbar and whose optical thickness at 0.8929 μm reaches values of 6 to 7.5. The single-scattering albedo of the NH_3 cloud particles is about 0.95 in

the visibly dark features with high 5-μm radiance. The optical thickness is consistent with the range quoted by the *West, Strobel and Tomasko* [1986] summary, and no further properties of the cloud or a deeper cloud were derived with this limited wavelength set.

Orton et al. [this issue], and *Stewart and Orton* [1997], analyzed a set of near-infrared data from Jupiter's solar reflection spectrum and derived an NH_3-level cloud near the 600- to ~350-mbar level. The optical thickness of this cloud is near 1.0 and only varies by about 20% between the "clear" hot spot and the adjacent "cloudy" Equatorial Zone (EZ) to the south. This variation is anticorrelated with the physical thickness of the cloud: the top of the cloud is near the 370-mbar level over hot spots and the 330-mbar level over the EZ. There was found to be no substantial sensitivity to clouds deeper in the atmosphere.

Collard et al. [1997] used high spectral resolution observations of CH_4 lines in 5-μm hot spots in 1996 August and December to determine the depth at which the 5-μm spectral lines of gaseous H_2O were being formed. Most of the "continuum" opacity is formed by the wings of gaseous H_2O lines, but a total opacity of 3 - 4 is required for the combination of NH_3 and NH_4SH clouds to attenuate the signal to the appropriate levels.

The analyses of much of the Galileo remote sensing data on 5-μm hot spots (for example, the high spatial resolution CCD images of a hot spot taken during the Europa-4 orbit in late December of 1996 by the Solid State Imager, SSI, experiment) are not mature as of this writing. (The term Europa-4 refers to a particular orbit of the Galileo Orbiter around Jupiter. This instance, for example, refers to orbit 4, in which the Orbiter was given a gravitational assist by passing close to the moon Europa.) The closest SSI study is the work of *Banfield et al.* [1997] on Ganymede-1 images around the Great Red Spot which included a region of high 5-μm brightness. Their model, relying on variations observed between 0.756 μm, a spectral continuum and 0.727 μm, a moderate CH_4 absorption band, is consistent with a 30-mbar to 40-mbar haze with $\tau = 0.05$ at 0.756 μm, below which is a 450-mbar to 200-mbar cloud with a 0.756-μm $\tau = 2.9$. These do not appear to change much laterally. Discrimination between various optically equivalent cloud models deeper in

the atmosphere is impossible, but the observations are consistent with a 2.5-bar cloud with $\tau = 0.5$ and single-scattering albedo of 1.0 whose variations most likely control the visible appearance of features in the atmosphere. Still deeper, some additional reflectivity is required and was modelled as a semi-infinite cloud with single-scattering albedo of 0.96; it is consistent with Rayleigh scattering.

Two other studies of similar regions have been completed recently using data obtained by the Galileo Orbiter Near-Infrared Mapping Spectrometer (NIMS). These used different model approaches and hot spot targets. The extensive analysis of a "warm spot" on the Ganymede-1 orbit encounter [*Weir et al.*, 1996; *Irwin et al.*, this issue] used a 3-cloud layer scheme. The deepest cloud layer was set to be physically thin and optimally placed near the 1.3-bar level, starting from an a priori solution given by the ~1.5-bar cloud peak of our preliminary nephelometer (NEP) results [*Ragent et al.*, 1996]. The need to match NIMS observations of the atmospheric reflectivity for wavelengths between 1.0 and 3.5 μm and thermal emission in the 5-μm region requires a small-particle uniform cloud at levels higher than the 1-bar level with larger particles in the lower part of the same cloud or deeper in a 5-bar H_2O cloud. Choosing the former, they derive a uniform cloud layer of 0.45μm radius NH_4SH particles with an optical thickness of 0.8 at 1.5 μm together with NH_4SH particles of 1.0-μm radius or larger with an optical thickness of 1.0 at 1.5 μm. The 5-μm optical thicknesses of these two layers are 0.05 and 1.00, respectively. Higher in the atmosphere, the NH_3 cloud layer composed of 0.75-μm particles is optimally placed at 0.69 bars, with an optical thickness of 1.3 at 1.5 μm and 0.08 at 5 μm. Finally an upper-level haze of 0.5-μm "tholins" is required near 0.30 bars, with a 1.5-μm wavelength optical thickness of 0.8 and a 5-μm optical thickness of 0.03. Thus, the 5-μm opacity is contributed essentially only by the 1.0-μm NH_4SH particles. Noting that a large-particle component is necessary to match the far-infrared thermal spectrum, they point out that 100-μm particles would have negligible effect on the 5-μm spectrum. Thus, a large-particle component cannot contribute significantly to the 5-μm variability in their model.

Roos-Serote et al. [1997, this issue], studied NIMS spectra from four 5-µm hot spots in the Ganymede-1, Europa-4, and Ganymede-7 orbital encounters, focusing on the 4.5- to 5.2-µm spectrum alone. For clouds, they derived only the total opacity above the 2-bar level, but mapped it, as well as NH_3 and H_2O humidity, in the targeted regions. Their models assumed only cloud opacity in the main cloud derived from our earlier results [*Ragent et al.*, 1996] and scaled its optical thickness in order to fit the observed spectral radiance properly. To simplify their analysis, they only examined areas of the atmosphere where the cloud opacity was likely to be low. Their retrieved cloud opacity reached a minimum of 0.5 for the clearest region of the very bright Ganymede-1 "hotmap" area (the brightest 5-µm hot spot observed), and it was correlated with low H_2O humidity but mildly anticorrelated with small changes of NH_3 humidity across the hot spot. The minimum opacity of this cloud layer in other hot spots does not vary very much from its value in the Ganymede-1 "hotmap" region, but it is larger, 0.87, for the "warm spot" region studied by *Weir et al.* [1997] and *Irwin et al.* [this issue].

Initial reports on the results of the Galileo Mission Probe experiments [see *Science, 272*, 837-860, 1996], as well as descriptions of the Probe instruments [see *Space Science Reviews, 60*, 3-610, 1992], have been published. This article describes the measurements and updates reports on the results of the Probe nephelometer experiment and initial attempts to interpret the data in terms of atmospheric and cloud properties.

2.0 Instrument Characteristics

A discussion of the measurement principles, the mechanical, optical and electronics design of the nephelometer instrument, tests, calibration and performance characteristics has been published elsewhere [*Ragent et al.*, 1992]. This section contains a short description of the instrument design and of laboratory tests and calibrations as well as in-flight tests.

The nephelometer instrument, tilted ~3 degrees downward, toward the nose of the Probe, was mounted on the instrument shelf of the Probe, projecting out through a closeout seal. An arm that held at its end the forward scatter mirror assembly (folded until deployed after atmospheric entry and aeroshell removal) extended the mirror assembly out about 23 centimeters from the Probe skin. The nephelometer recorded the light scattered from an incident light beam at five angles (5.8°, 16°, 40°, 70°, and 178°) from the forward direction by particles in the atmosphere that flowed through sampling volumes in the near vicinity of the descending Probe. (Contribution from light scattered by atmospheric gases, Rayleigh scattering, was too small to produce any changes in the recorded signals.) The scattering cross sections derived from these data were then compared for best fits with the calculated scattering from model aerosols to attempt to obtain a plausible description of the particles assumed to have scattered the light. The desired results included the parameters of the particle size distribution and, if possible, indications of the particle indices of refraction, including absorption, and whether the particles were liquid or solid.

The desire to obtain more frequent measurements during early descent when the descent velocity was large led to a different nephelometer data format than that used by the Probe data system [see *Ragent et al.*, 1992, for a fuller discussion]. Measurements were obtained every three seconds for the first 10 measurements, every four seconds for the next 10 measurements, etc. until a time of 12 seconds for each of 10 measurements was reached. After this the time per measurement was reduced to eight seconds for the rest of the Probe descent. The data were recorded into the internal memory of the instrument as 10-bit words, but these bits were furnished to the Probe data system in eight-bit sequences, as required for the Probe data format.

In addition to the main scattering data for each angle, measurements of any optical surface contamination and four values of the 16° channel electronics gains, each equally spaced in time between reported scattering measurements, were recorded at least once during each kilometer of descent. A number of "housekeeping" measurements, recorded

less frequently, were also included. These included the monitoring of three temperatures within the instrument, a reference voltage, three light source outputs, angular alignment of the forward scatter mirror assembly, and six electronics channels offsets.

The instrument channel sensitivities were calibrated using three independent techniques. These involved (a) scanning through the sensitive volume for each scattering angle with a well documented scattering (or reflecting in the case of the 178° channel) target and integrating the responses over the scan [*Pritchard and Elliott*, 1960], (b) recording the scattering channel responses in a "standard" aerosol" particle chamber that was documented using other types of well calibrated instrumentation, and (c) attempting to obtain the scattering channel responses due to Rayleigh scattering in a chamber containing a gas (freon at high pressure). The results of these calibrations indicated that the most reliable and accurate method was the scanning technique, yielding estimated accuracies of about five percent.

In addition to the extensive room temperature calibrations, a large number of pre-launch tests were performed on the instrument in order to characterize and understand its behavior. Before installation of the instrument on the Probe, these included (a) both steady state and transient temperature tests covering the pre-flight specified ranges of -20° to +50° C to measure the effects of these temperature environments on baseline offsets, sensitivities of each channel, actual light output and polarization characteristics of the light sources, light source monitor outputs, and the alignment and contamination detector readings, (b) wind tunnel tests and model calculations to establish the flow paths of particles around the Probe as a function of Probe descent velocity and particle size and mass, (c) tests to pressures ranging from 0 to about 6 bars to establish the sensitivity of the instrument to pressure, and to check the integrity of the pressure seals of the instrument electronics unit, (d) ambient light tests, (e) vibration and acceleration tests, and (f) actual tests in the earth's atmosphere measuring particles in atmospheric conditions such as in fogs.

A large number of tests of the instrument were conducted during the assembly of the Probe and its integration with the Galileo Orbiter. Tests during Probe assembly measured the health and status of the instrument (a) with all of the channels optics covered and its deployable arm folded, or, (b) with the arm deployed, optics open, and a simplified modification of the scanning calibration technique using a limited number of fixed target positions.

Two test targets aligned with the nephelometer were mounted on the aeroshell assembly that held the atmospheric entry heat shield enclosing the Probe. These targets provided reference scatter signals to the nephelometer for checking its condition after launch, during the interplanetary cruise phase and before the Jupiter atmospheric entry. Tests conducted before launch, shortly after launch, and during the cruise phase, verified the health and viability of the instrument to make measurements in Jupiter's atmosphere.

During the Probe descent in the Jovian atmosphere, the measured instrument temperatures were found to exceed the originally expected and specified ranges and rates of change. Recorded temperature values were in the range of about -50° to >100° C and changed at rates of up to 10° C per minute. Differences of up to more than 10° C at a given time between the forward and backward scattering channel source regions were noted. There were also indications of much more extreme temperature differences between these regions and the region containing the alignment system source closer to the Probe wall, implying strong temperature gradients. Accordingly, after encounter, temperature tests covering much of this range, i.e. from about -60° to +60° C were performed on the flight spare Engineering Unit (EU), to better characterize the data received from the flight instrument. Although these tests were useful in establishing the response of the flight instrument, the data from these tests had to be used cautiously since there were, undoubtedly, differences between the flight unit and spare flight unit responses. In addition, it proved to be difficult to simulate the descent conditions fully, including the rates

of change and details of the variation of temperatures with time in different portions of the instrument.

3.0 Data Processing

3.1 Discussion of Processing of Telemetry Data Records

The Probe experimental data relayed from the Probe to the Orbiter during Probe descent were transmitted by the Orbiter to the Deep Space Network telemetry receiving stations, and were processed and presented to the experimenters by the Galileo Probe Project Office. These records consisted a data stream containing annotations, timing information and a series of 8-bit words arranged according to the designed minor frame format of 64 eight-bit words. Almost all of these data were received in a near-redundant form from the so-called A and B strings of the Probe data system. Each Probe minor frame contained five eight-bit words assigned to the nephelometer experiment. Because the nephelometer internal format required 800 bits to record one complete cycle of 10 measurements during descent, 100 minor frame words from 20 Probe frames were required for each cycle of ten nephelometer measurements. The complete data cycle for all of the measurements and ancillary data was then reconstructed from the 100 eight-bit words.

The nephelometer data frame contained a synchronization word, housekeeping data measurements, and 10 scattering data records, all included in the 800 bits. These data were recorded in the form of compressed 10-bit words, each consisting of a sign bit, three bits for the power of four exponent and six bits for the six most significant bits of the pertinent record.

The experimental data records received from the Galileo Probe Project Office were first processed by separating out the applicable nephelometer words, applying a reordering program to each of the words received so as to reconstruct the 800-bit instrument data frame

and each of the 10-bit data words, and applying an appropriate decompression algorithm to obtain the values of the data in raw data counts.

The beginning time of each nephelometer data frame and the time for each measurement in the data frame were referred to the time for the beginning of the Probe minor frame zero (MFZ), nominally specified as the start of descent. The ambient atmospheric pressure, temperature, density, and Probe altitude were obtained by reference to the results obtained by the atmospheric structure instrument (ASI) experiment [*Seiff et al.*, this issue], and each measurement was then tabulated as a function of time of measurement, ambient pressure, temperature, density and altitude.

3.2 Estimate of Measurement Accuracy

Errors introduced by the telemetry link and telemetry data processing are caused by modifications of, the addition to, or loss of bits from the data stream. In this experiment, there were substantial redundancies of data transmission, both from the redundancy in the design of the Probe data system and multiply repeated transmissions of the recorded data stream from the relay system aboard the Orbiter. Thus, it is believed that the telemetry errors were essentially eliminated and that the data received by the experimenters was very closely, if not exactly, the same as the data delivered by the instrument to the Probe data transmission system.

Granulation uncertainties are introduced by the digitizing and data compression schemes used in this experiment. For example, for signals in the range from 0 to 64 units, data were reported in intervals of 1 unit, whereas from from >64 to 256 the interval increased to 4 units, from >256 to 1024 to 16 units, and so forth. Thus a reading of 300 units would be recorded as 288 with an uncertainty of +16 units. Since signals lay between a reported level and its additional least significant value, these non-statistical uncertainties were always positive, and varied from about +1.6% to +6.25% of its value depending on the magnitude of the signal.

Attempts were made in the laboratory to document the noise in each signal channel as a function of instrument temperature. Typical results indicated that in the least sensitive 5.8° channel the noise frequency distribution had a full width at half maximum of a few counts whereas for the most sensitive channel, the 178° channel, the full width at half maximum was about 10 to 20 counts at room temperature.

As discussed below, the behavior of the baseline offsets with temperature in the flight data appeared to differ markedly from the behavior of these offsets in pre-flight tests. As a result, an alternate empirical technique for applying offset corrections was used. It is believed that, using the assumptions and recorded quantities discussed below, the major uncertainty in the baseline magnitudes arises from the granulation error of the recorded quantities. The processing used, the subtraction of the baseline reading for the minimum signal level (ostensibly at the base of a cloud structure) at a specified measured pressure from the recorded signals in its vicinity, and the subseqent use of these quantities, have uncertainties determined from calculating the error propagation. The uncertainty in the baseline drift itself is therefore not considered in this calculation of the uncertainties in the measurements.

Sampling statistical errors can be estimated for a given density of particles, n, from the expression for the probability, $P(N)$, of having N particles in sampling volume V at any instant. The expression for $P(N)$ is given by,

$$P(N) = (nV)^N (N!)^{-1} \exp(-nV) \tag{1}$$

For this distribution, the average value is nV and the standard deviation is $(nV)^{1/2}$, so that the percent standard deviation from the average is $100\ (nV)^{-1/2}$. In our case, the smallest sampling volume was >575 cm^3 for the 70° channel, corresponding to 4096 independent volume samples in the most sensitive range, so that the sampling standard deviations varied from less than 13% at $n = 10^5$ m^{-3} to less than 1.3% at n $= 10^7$ m^{-3}.

Estimates of the the accuracy of the measurements (exclusive of particle sampling statistics) included (a) considerations of telemetry errors, (b) granulation uncertainties due to digitizing and data compression schemes used here, (c) noise in each channel, (d) calibration uncertainties, and (e) baseline drifts. Factors (c), (d) and (e) must include corrections for instrument temperature and other environmental factors.

The percent uncertainty is equal to:

$(100/\text{signal})$ {[(telemetry uncertainty)^2 + (granulation uncertainty)^2 + (noise uncertainty)^2 +

(base line drift uncertainty)^2]$^{1/2}$ + (calibration uncertainty)}

The full scale ranges for the 5.8˚ channel extended from 4.9×10^{-5} m^{-1} sr^{-1} for the most sensitive range to 3.11×10^{-3} m^{-1} sr^{-1} for the least sensitive range, and, correspondingly, for the 178˚channel, from 5.73×10^{-7} m^{-1} sr^{-1} to 3.66×10^{-5} m^{-1} sr^{-1}. For these channels the percent uncertainties in the most sensitive ranges, exclusive of the calibration uncertainty (estimated to be about 5%), amounted to about 8% and 16% of the full scale ranges, respectively. For larger signals in signal ranges successive to the most sensitive range, each with a full scale value equal to four times larger than the next smaller full scale value, the non-calibration uncertainties decreased with increasing full scale values to a final minimum of 1.6% of full scale in all channels.

3.3   Presentation of Processed Raw Data

The decompressed raw data counts for the instrument status, i. e. housekeeping, data, are plotted as a function of ambient pressure in Figures 1, 2, and 3. Figure 1 is a plot of the internal instrument temperatures near the forward scatter laser injection diode (LID) light source, near the backward scatter LID light source, and inside the pressure tight electronics container, as well as a plot of the measured ambient atmospheric temperature (Seiff, private communication). Figure 2 shows plots of the readings of monitors of the light output of the forward scatter, backward scatter, and the contamination (and alignment) light sources.

Figure 3 displays the data recorded for the optical surfaces contamination detector and the outputs from the four quadrants of the alignment detectors. The contamination monitor output is the sum of the outputs of the four quadrant detectors used as a time-shared detector with the less frequently taken alignment measurements. The gain of the 16° scatter channel, monitored four times during the period of each measurement of this channel, is not presented here because the scatter signal magnitudes were low during the entire descent period and the value of the gain remained constant at its highest value.

The directly processed records of the raw outputs from the five angular scattering channels during the Probe descent are plotted in Figure 4. Expanded versions of these records are also shown in Figures 5a, 5b, 5c and 5d.

3.4 Reduction of Raw Data to Physical Quantities

The raw data counts recorded in the scatter channel data were to be reduced to scattering cross sections, $F(\theta) = N_0 (d\Sigma/d\Omega)_\theta$ $m^{-1}sr^{-1}$, where N_0 is the density of particles and $d\Sigma$ is the differential scattering cross section for scattering from the incident beam into solid angle element $d\Omega = sin\theta\, d\theta\, d\phi$ at scattering angle θ. This was to be accomplished by subtracting the appropriate channel baseline offset counts, as determined in the preflight calibration tests for the measured instrument temperature, from the raw data counts of each channel, and then applying the calibration coefficient for each channel, in units of $m^{-1}sr^{-1}count^{-1}$, for that temperature. Unfortunately, it proved to be very difficult to make accurate straightforward corrections to each channel's baseline offsets because of the severe temperatures, rapid temperature excursions, and temperature gradients experienced by the instrument during descent, outside of the pre-flight calibration ranges. For the very small signals often measured, the extrapolated baseline corrections appeared to be much larger than the signals themselves. In addition, the behavior of the baseline offsets with temperature for the flight data appeared to be different from the behavior of these offsets with temperature evidenced in the preflight tests. The reasons for these differences are not

completely understood at present, but might be attributable to the large temperature gradients and the rapid rates of temperature change.

As a result, a different approach to reducing the raw data to physical quantities was used. This technique assumed that in regions exhibiting appreciable scattering signals, the minimum values of data at the base of such regions, as noted by simultaneous minima in at least three of the scattering channels, indicated a lower boundary to scattering structures, structures which were presumably composed of particles in the atmosphere. The value of this minimum reading in each channel was taken to be that for a clear atmosphere, free of particles, and to be the applicable offset for the region near the boundary. It was assumed that this offset was essentially constant for measurements taken near this boundary, and that signals greater than the offsets in these lower boundary regions were due to the particulate scattering medium. Temperature compensated calibration coefficients, derived from pre-flight flight unit calibrations, were extended using the results of post-flight spare flight unit laboratory tests. They were then applied to these baseline "corrected" data in the applicable altitude regions. It is recognized that this process may ignore the contribution from extended scattering structures of appreciable thickness that vary slowly with altitude and may even underlie the more sharply varying less extended structures, and that using the fixed offsets introduces errors into the offsets for reduced data measurements made at some distance from the assumed minimum. It appears, at least for the most pertinent signal regions considered here, that this method yielded reasonable estimates of the amounts of scattering attributable to these structures.

Curves of derived cross sections for scattering at the five scattering angles as a function of pressure are shown in Figures 6a, 6b, 6c and 6d. Also shown in Figures 6b, 6c and 6d are estimates of the errors associated with these derived cross sections including digitization uncertainties, estimates of noise in each channel (derived from preflight and cruise phase tests) and propagated errors associated with the manipulations of the data. Systematic errors due, for example, to uncertainties in calibration, have not been indicated here.

As an example of the close correlation of signals in the signal channels, Figure 6b shows the cross section data from the 5.8°, 16°, 40°, and 178° channels for the ambient atmospheric pressure region of about 0.9 to 1.4 bars, superposed onto the same scale of ordinates by multiplying the data from each channel by an appropriate constant factor, as indicated.

The general similarity in the shapes of these signals lends some confidence in the constancy of the assigned offset for each channel over much of this range of measurements.

4.0   Data Reduction and Discussion

4.1   Housekeeping Data and Implications

a) Temperature Sensors

The temperature profiles measured by the sensors mounted near the forward and backward sources indicate that the internal Probe temperature and the instrument temperature were very strongly influenced by the external atmospheric temperature. The first temperatures recorded by the instrument sensors, approximately 1° C, were at a time prior to Probe separation from the aeroshell, and were about as expected from the aeroshell environment, including its heaters. Subsequent temperature behavior indicated a very strong coupling of the instrument temperatures to the external atmospheric temperature and also indicated that the Probe housing was providing much less thermal isolation than had been expected. Figure 1 shows plots of instrument temperatures and atmospheric temperature as a function of time from minor frame zero (MFZ) (t = 0 at p ~ 0.41bar), and shows that the instrument temperatures, lagging by about 25°, followed the rising atmospheric temperature up to over 100° C fairly faithfully after cooling down to about -50° C for about the first 700 seconds. Other Probe instruments and the shelf on which the instruments were mounted also exhibited similar temperature-time excursions.

b) Source Monitors

The outputs from the monitors of the outputs of the forward and backward scatter (LID) sources, Figure 2, showed variations that reflected the measured temperatures of these sources. The high temperatures produced reductions in source output from about 50° C onward to catastophic decreases when the sources reached temperatures of about 60° to 70° C, at ambient atmospheric pressures of about 12 to 13 bars. The beginning of these decreases thus marked the termination of any useful measurements by the instrument at an atmospheric pressure of somewhere between about 10 to 13 bars.

The source monitor of the contamination and alignment measurement source also documented the behavior of this light emitting diode (LED) as a function of temperature (see Figure 3). This source and its monitor were at locations much closer to the Probe skin than the other source monitors and temperature sensors, and showed a sharp increase in output, up to saturation of the monitor before the first 100 seconds of descent. Based on preflight test data and the results of post-flight low temperature tests on the spare flight instrument, we believe that this monitor behavior indicated that the region of the instrument containing this source, and that, incidentally, contained the instrument's backward scatter channel detectors, was very cold. In fact, it was probably much colder than indicated by the scatter channel sources temperature monitors that were mounted inboard, much farther from the Probe skin. This contamination channel source monitor remained saturated until after 900 seconds of descent after which its readings decreased. It continued to indicate very high source outputs, until the readings decreased to more nominal values and leveled off at times of ~1000 to ~1500 seconds after MFZ (~4.1 to ~6.8 bars). They remained nominal until final decrease after times of ~2300 seconds (~12 bars).

c) Contamination and Alignment Channel Records

The contamination channel recorded the readings of the sum of the outputs of the four quadrants of the alignment detector to light pulses generated particularly for this measurement by the LED source. The collimated source beam was directed out through the outboard side of the backscatter channel assembly, reflected from a flat mirror mounted on

the deployed mirror assembly onto the quadrant detector mounted inside the backscatter channel unit. Readings deviating from nominal, and unusual variations of these readings in time were, presumably, to arise from changes in the optical path followed by the light beam, indicating that the optical surfaces of the mirror or windows had become coated by deposits of condensates from the atmosphere, even though during descent these surfaces were electrically heated in an attempt to prevent such depositions. The readings of this monitor (see Figure 3) seemed to indicate appreciable deposition during the early descent period, covering the period from about 30 (~0.49 bars) to about 350 (~1.42 bars) seconds after which these deposits appeared to evaporate for the next 700 (~4.4 bars) seconds, leading to a 'clear' system until the monitor stopped functioning after about 2300 (~12 bars) seconds. However, subsequent post-flight laboratory tests of the spare flight unit demonstrated conclusively that the observed behavior of the contamination monitor channel was the result of the response of the quadrant detector system to the unusually high outputs from the LED light source caused by its extremely low temperatures at this time. This amount of light led to partial long-time-constant saturation and biasing of the quadrant detectors, reducing the apparent output of these detectors to the subsequent light pulses, and simulating the appearance of contamination. At this time we conclude that there is no conclusive evidence that any contamination of the optical surfaces took place at any time during descent.

The behavior of the alignment monitors (Figure 3), also indicated the variations described above. Again, and with the possible exception of a small difference in the behavior of one of these four detectors at 1500 to 2300 seconds (~6.8 to >12 bars), there was no indication of any change in the effective scatter angles caused by arm motion or mechanical distortions.

4.2 Description of Scatter Channel Signals in Various Altitude Regimes

a) Pressure region of 0.46 to 0.59 bars (altitudes of 17.3 to 12.4 kilometers above the one bar atmospheric pressure level, measurement numbers 6 to 20) (See Figure 6a).

The first valid nephelometer readings occurred at deployment at an ambient pressure level of about 0.46 bars (altitude ~17.3 kilometers above the altitude at which the ambient pressure is one bar). As the Probe descended, the magnitudes of the signals decreased from those measured at 0.46 bars to a minimum value at a pressure level of about 0.52 bars, and then the signals exhibited several peaks, correlated in all of the instrument channels, down to a pressure of about 0.58 bars. Equilibrium thermodynamic calculations, using atmospheric concentrations of NH_3 vapor equal to "solar" concentration, had previously predicted the presence of a cloud of ammonia particles above a cloud base at approximately 0.6 bars [Weidenschilling and Lewis, 1973; Atreya and Romani, 1985; Atreya, 1986]. Other experiments aboard the Probe [Sromovsky et al., this issue; Seiff et al., this issue] have also indicated the presence of a cloud at and above these pressure levels. Using equilibrium cloud simulation Atreya et al., 1997, have calculated the presence of an ammonia-ice cloud based at 0.5 bars assuming an NH_3 concentration of 2.2 x 10^{-6} by volume (0.01 solar). Best fits to the data obtained by the Probe Net Flux Radiometer (NFR), also indicate a derived NH_3 abundance of the order of a percent of solar at pressures of 0.5 bars [Sromovsky et al., this issue]. This value is also in accord with analyses performed on Earth-based and Galileo Orbiter NIMS observations of hot spots at Galileo Probe entry site latitudes [Stewart et al., this issue; Roos-Serote et al., this issue; Irwin et al., this issue]. The nephelometer signals at these altitudes indicate a decreasing particle concentration with pressure, with some evidence of vertical inhomogeneities in structure near its base. Such behavior for cloud bases is not uncommon for Earth clouds, as usually associated with local atmospheric dynamics as well as microphysical cloud considerations of condensation, coagulation and/or coalescence, and precipitation. Such considerations also affect actual observed cloud mass concentrations which are sometimes at least an order of magnitude smaller than predicted from equilibrium calculations. Although our experiment does not show a sharp lower boundary for such an NH_3 cloud at these

altitudes, we have interpreted the measurements in this region to indicate particles belonging to the lower portions of the predicted NH3 cloud.

b) Pressure region of 0.60 to 0.75 bars (altitudes of 11.9 to 7.0 kilometers above the one bar pressure level, measurement numbers 21 to 32).

Although some very small correlative signals among several channels, that may be associated with the overhead NH3 cloud, have been found in this pressure range, the atmosphere appeared to be clear of any notable amount of particulate matter.

c) Pressure region of 0.76 to 1.34 bars (altitudes of 6.5 above to 7.8 kilometers below the one bar pressure level, measurement numbers 33 to 60). (See Figure 6b.)

The first portion of this region starting at about 0.76 bars (6.5 kilometers above the one bar pressure level, measurement number 33) shows an increasing concentration of particles, the beginning of a buildup that reaches several more prominent structured layers of particles starting at a pressure level of about 1.00 bars (0.1 kilometers below the one bar pressure level, measurement number 46). This buildup appears to be the top part of a region in which the equilibrium thermochemical calculations mentioned above [*Weidenschilling and Lewis*, 1973; *Atreya and Romani*, 1985; *Atreya* 1986] have predicted the existence of a cloud of particles comprised of a compound of NH3 and H2S, the so-called ammonium hydrosulfide (NH4SH) cloud . The major portion of the structured layers in this structure lies below this buildup, and consists of two main overlapping layers, the first extending from about 1.00 to 1.14 bars (0.1 to 3.4 kilometers below the one bar pressure level, measurement numbers 46 to 52) and the second, denser, sharply-terminating layer from 1.14 to 1.34 bars (3.4 to 7.8 kilometers below the one bar pressure level, measurement numbers 52 to 60). *Atreya et al.*, 1997, have calculated that an NH4SH cloud, based at 1.34 bars in the Jovian atmosphere, can be identified with an assumed mixing ratio for H2S of 1.8×10^{-7} (~6 x 10^{-3} solar). This H2S concentration is in fair accord with the upper

limit mixing ratio of H_2S of 10^{-6} reported by the Galileo Probe Mass Spectrometer (GPMS) experiment [*Niemann et al.*, this issue] for pressures less than 3.8 bars, and the upper limit of 3.3×10^{-8} at pressures of less than 0.8 bars reported from Earth-based observations [*Larson et al.*, 1984]. The GPMS results also indicate dramatically rising mixing ratios for H_2S as a function of increasing pressure.

Only upper limiting determinations for NH_3 concentrations of 7 and 10 times solar at pressures of 11.7 and 20.2 bars are now available from the GPMS results [*Niemann et al.*, this issue]. *Folkner andWoo* [this issue] have reported that analyses of the radio signal directly received on Earth from the Probe as it descended in the Jovian atmosphere have also yielded a measure of the NH_3 concentration as a function of pressure. Their analyses show an increase in NH_3 concentration with depth for pressures greater than about 4 bars, and have yielded values of NH_3 abundance somewhat smaller than, but within an order of magnitude of solar abundance at pressures less than about 2 bars. This lower pressure value must be considered with caution since their results at low pressures are the most noisy and unreliable of their measurements . For the pressure range of about 0.7 to 1.5 bars, and using the values of de Pater and Mitchell [1993] for pressures of ≥ 4 bars the Probe NFR results (*Sromovsky et al.*, this issue] are fit with abundance values of several percent of solar up to about 10 percent of solar, of the same order as the radio signal measurement results of Folkner and Woo [*Folkner and Woo*, this issue]. The Probe appears to have entered a "dry" atmosphere that may have been experiencing some lateral mixing with depth, a proposal that would also explain the increasing concentrations of NH_3 and H_2S (and H_2O) with depth.

The calculated cloud mass concentrations obtained from the equilibrium thermochemical model calculations mentioned above, although probably considerably larger than those derived from the nephelometer experiment data (see Tables I, II and III), are not unreasonable, considering the simplified model used for the calculations that, for example, ignores atmospheric motions and cloud microphysical processes.

d) Pressure region of 1.37 to 1.72 bars (altitudes of 8.4 to 15.0 kilometers below the one bar pressure level, measurement numbers 61 to 72). (See Figure 6b.)

. Several very tenuous and spatially thin layers of particles are apparent at pressure levels of 1.40 and 1.52 bars (altitudes of 9.0 and 11.4 kilometers below the one bar pressure level, measurement numbers 62 and 66), and a denser sharp layer is evident at a pressure of 1.65 bars (13.8 kilometers below the one bar pressure level, measurement number 70). The composition of these layers is not at all clear at present. It is possible that these wispy layers may be associated with the more substantial, but still modest, cloud directly above, whose particles' composition was tentatively associated with NH_3 and H_2S compounds, and are simply detached layers, as frequently occurs for Earth clouds. Alternatively, it is possible, assuming a very small local vapor pressure of H_2O, that these layers may be evidence of the presence of a very feeble water-ice "cloud". For the sharp layer at 1.65 bars *Atreya et al..* [1997], using equilibrium thermochemistry, have calculated the possibility of such a composition, assuming an H_2O mixing ratio of 10^{-4} solar. Again, this composition is consistent with the low limits on the concentrations of H_2O at these pressures inferred from the analyses of data from other Galileo Probe and Orbiter experiments [*Niemann et al.,* this issue; *Roos-Serote et al.,* 1997]. The largest density of material condensed in these layers, as estimated from the nephelometer results, is small (Ragent, unpublished), even smaller than the low values that would be predicted from equilibrium calculations. While not ruling out the possibility of H_2O condensates at these pressures, and because of the proximity of these layers to the structure above, we are slightly inclined at present to favor associating the composition of these layers with that of the particulate structure overhead.

e) Pressure region of 1.76 to 4.9 bars (altitudes of 15.6 to 52.2 kilometers below the one bar pressure level, measurement numbers 73 to 150). (See Figure 6c.)

The upper portion of this region, say from 1.8 to about 2.5 bars, appears to be the beginning of the buildup of a structure that is composed, in general, of a series of very tenuous overlapping layers that join together to form a feeble but relatively extensive continuous structure extending to, perhaps, as low as or lower than 4.5 bars. However, in this region temperatures well below our design specifications were experienced by our instrument, and the magnitudes and variation with time of baseline drifts and channel sensitivity variations are uncertain. We have attempted to use the extensive post encounter laboratory tests of our spare flight instrument better to define the performance of the flight instrument using extrapolations and insights gained from these tests, but many uncertainties remain. The existence of particle structures of some significance in this region is certain, as evidenced by the sharp, simultaneous variations in the readings obtained in the 5.8°, 16°, and 178° channels at pressures of 2.1bars, and of the 5.8°, 16°, 40° and 178° channels at 3.5 bars (see Figures 6c and 6d). Although the exact baseline variation is difficult to establish, the sharp variations in these channels, especially the correlation of the 5.8°, 16° and 40° channel behavior with that of the 178° channel is compelling, since these two sets of data come from essentially two separate instruments, and the common digital electronics used by these two sets of channels never experienced the extreme conditions as the sensor heads. In addition, the relative magnitudes of these changes in the various channels are in accord with those that would be expected from particle scatterers with reasonable optical properties.

The sharp variation at the 3.5 bar level makes it tempting to assume that this indicates the base of a layer of a cloud structure, and that subsequent small signals detected at even greater pressures are due to particulate matter associated with but detached from this structure. Although the magnitudes of the signal variations, especially in the 5.8°, 16°, and 178° channels, were above any instrumental, digitization, or sampling errors, the signals are in general small, and the overall magnitudes of the effects of this tenuous "cloud" may well be minor. An estimate of the typical extent of this layer is that it extends from roughly 2.4

down to about 3.6 bars (26.2 to 39.8 kilometers below the one bar pressure level, measurement numbers from 90 to 117), or to a bit higher pressure.

Equilibrium calculations of the abundance of H_2O required for the formation of an H_2O-ice cloud in this region. based at 3.6 bars, give values of the order of a tenth of the solar abundance value [*Ragent*, 1997 unpublished; *Atreya*, personal communication], far outside the values reported by measurements from other Probe and Orbiter experiments [~ 5 x 10^{-4} solar for p < 3.8 bars from the Probe GPMS results (*Niemann et al.*, this issue) and about 10^{-4} to 10^{-2} solar for p = 4 bars in different portions of the hot spot (and less for p < 4 bars) derived from modeling of the Orbiter NIMS results (*Roos-Serote et al.*, this issue)]. However, modeling calculations to fit the Probe Net Flux Radiometer (NFR) measurements yield values of H_2O abundance of about 0.1 solar [*Sromovsky et al.*, this issue] at a pressure of 3.6 bars, using an NH_3 profile (based on the measurements of *de Pater and Mithchell* [1993]), which proves to be similar to that of *Folkner and Woo* [this issue] in the pressure range of 2.2 to 4 bars. It should be noted, that thermochemical equilibrium calculations predict several orders of magnitude more condensed H_2O than is consistent with the optical scattering measured by the nephelometer.

At present we are uncertain of the chemical or physical nature of the species giving rise to the signals observed in this region. Several possibilities have been suggested, but, as yet, none can be completely verified from existing measurements. One possibility is that this structure really is a tenuous water-ice haze. Various explanations for the reduction in the amount of particulate matter in a water cloud from that predicted from thermochemical equilibrium at this altitude have been proposed. For example, *Engel et al.* [personal communication], have developed a 1-dimensional model that includes considerations of microphysical processes and precipitation. Assuming that a water cloud had formed at these altitudes at any time (a somewhat unlikely event considering the low measured H_2O concentrations and the uncertainty of the existence of a cloud base) they have calculated that, "a subsidence velocity of 1 m/sec reduces the cloud mass by about 2 orders of magnitude,

and places the cloud peak at an altitude of 220 K (~2.4 bars) instead of 270 K (~4.7 bars). A 1.5 m/sec subsidence reduces the cloud density by almost 4 orders of magnitude and a subsidence velocity of 2m/sec makes the cloud disappear."

Another suggestion is that perhaps we are sampling material which is being transported laterally from much wetter conditions outside the downwelling region. Observations made by the Galileo Probe Mass Spectrometer [*Niemann et al.*, this issue] show an increase of the abundances of H_2O and H_2S with depth, and interpretation of the larger than expected Probe signal attenuation as an increase of the NH_3 gas abundance with depth [*Folkner and Woo*, this issue] is consistent with this process [see also *Atreya et al.*, 1997). In fact, it is expected that lateral motions will eventually become as strong as the downwelling motion assumed to be characteristic of the hot spot. This possibility might even be enhanced by the location of the Probe entry site near the southern perimeter of the hot spot [*Orton et al.*, this issue], as the Orbiter NIMS experiment has detected clear evidence of large variations of H_2O vapor going from the center toward the periphery of 5 μm hot spots [*Roos-Serote et al.*, this issue]. Further explanations for the local atmospheric dynamics and variations of the concentrations of condensibles measured by the Galileo Probe instruments at its entry site, and Galileo Orbiter and Voyager measurements in hot spot environments are now appearing, as, for example, have been proposed by *Showman snd Ingersoll* [1997; submitted to *Icarus*], and by *Baker and Schubert* [1997].

An unusual suggestion [*O. B. Toon*, personal communication] involves the possible condensation of water in a very clean atmospheric situation almost totally free of cloud condensation nuclei that could produce heterogeneous nucleation. If the vapor pressure in such a region is low enough so that homogeneous nucleation is rare, then the few such events that occur can result in the rapid growth of particles so large that they produce only very small signals in experiments designed to detect normal particulate scattering. Such explanations have been proposed to explain effects in the Earth's atmosphere, the so-called "rain in a cloud-free atmosphere" [*Ackerman, Toon and Hobbs* 1993].

Finally, the scattering in this region observed in this experiment may be due to an, as yet, unspecified species.

f) Pressure region greater than 4.9 bars (altitudes of more than 52.2 kilometers below the one bar pressure level, measurement numbers greater than 150). (See Figure 4.)

Although a number of significant correlations among several channels for very small signals were observed, no significant particulate structure extending over any appreciable altitude range was evident at pressures greater than 4.9 bars down to pressures of at least about 10 bars to the instrument failure at about 12 bars.

4.3 Data Reduction. Determination of Particle Characteristics and Cloud Properties

Introduction. The nephelometer uses measurements of the angular distribution of scattered light to characterize particles. There are limitations inherent in attempting to use nephelometer data to infer particle characteristics and cloud properties. The maximum particle size that can be characterized by such an instrument is limited by the angular width to the first particle diffraction pattern minimum and the smallest angles sampled by the instrument, and in our case amounts to a particle size of about 10 μm. Particle size distributions containing appreciable numbers of larger particles can produce data that may only lead to particle size descriptions as "large".

Factors such as sphericity, non-sphericity, inhomogeneity, appreciable voids (fluffy particles), inclusions, coatings, mixtures of allotropes, appreciable absorptivity, etc., influence the scattering behavior of particles. The differences in scattering behavior among such particles may cause difficulties in attempting to characterize the particles using scattering measurements made at only a few angles. However, calculations and some measurements of the scattering from such particles, discussed below, have shown that, for a given refractive index and similar nominally sized distributions, the scattering from

nonspherical particles, averaged over orientation, does not differ radically from that of spherical particles in the forward direction out to scattering angles of about 40°. Generally, at intermediate and larger angles (~70° to 150°) non-spherical particle phase functions averaged over orientation do not show the detailed structure associated with the phase functions for spherical particles, and often tend to deviate from those for spherical particles. Scattering at very large (~178°) angles also shows different, usually lower, values for non-spherical particles (see, for example, *Pollack and Cuzzi*, 1980; *Zerull and Giese*, 1974; *Zerull, et al.*, 1993; *Schuerman*, 1980, *Schuerman et al.*, 1981; *Mischenko and Travis*, 1994; *Mischenko et al.*, 1997; *West, Tomasko and Doose*, 1994; *West et al.*, 1997). In addition, absorption in the scattering particle may tend to modify the scattering phase function from that for the same particle without absorption to a greater or smaller degree, but generally in a similar manner.

Mie theory is used extensively for calculations for the scattering from spherical and near-spherical particles, spheroids and cylinders; however, for non-spherical and aggregate particles, several popular numerical algorithms are the discrete dipole approximation (DDA), which is limited by practical considerations to particles with equivalent radii of the order or smaller than the incident light wavelength, [*Purcell and Pennypacker*, 1973; *Draine*, 1988; *Goodman, Draine and Flatau*, 1990; *Draine and Flatau*, 1994], and T-matrix techniques [*Mischenko*, 1993; *Mischenko and Travis*, 1994; *Mischenko et al.*, 1997]. Using the DDA method *Xing and Hanner* [1996] and *Yanamandra-Fisher and Hanner* [1997] have done detailed studies of the effects of shape parameters on optical scattering, as applied to comet dust. A similar study for a "variety of particle shapes and sizes up to equivalent-volume size parameter $X = 2\pi r/\lambda = 8$, etc.", and a log-normal size distribution were performed by *West, Tomasko and Doose* [1994]. *West et al.* [1997] have also performed laboratory measurements of scattering phase functions and polarizations for mineral dusts for particles with equivalent-sphere radii from a few tenths to about 10 μm. They find that the experimental results compare favorably with scattering phase functions calculated for

spheroids with a distribution of axial ratios, sizes, random orientation and appropriate indices of refraction.

Using the DDA approach we have also run a suite of cases including five regular shapes (sphere, cylinder, ellipse, hexagon and tetrahedron) using two different size parameters and several values of the imaginary refractive index. Results of one such set of calculations is shown in Figure 7. As in some of the publications mentioned above we find that shape effects are negligible when the particle dimensions are smaller than the wavelength. For larger particles there are essentially small differences among the phase functions for the five regular shapes in the forward scattering direction; however, the enhancement in backscatter, although almost always smaller than for a spherical particle, is greater for equidimensional particles such as sphere and tetrahedron and lower for elongated particles such as the ellipse, cylinder and hexagon. In contrast, when the particle size is increased to be comparable to, or larger than, the wavelength of light, the phase functions of the various shaped particles exhibit more differences in structure. In the forward scatter direction, particularly from 0 to 70 degrees, the phase functions of all shapes behaved similarly, elongated particles demonstrating slightly sharper forward diffraction peaks. However, at intermediate scattering angles (70 to 150 degrees) and in the backscatter direction, there are distinct structural differences in the phase functions and the behavior of the non-spherical particles backscatter was varied. The backscatter enhancement decreased for elongated particles and was greater for equidimensional particles such as sphere and tetrahedron. As the particle size became much larger or if an aggregate composed of these particles with an effective size parameter greater than the wavelength of light was used, we find that the behavior of the scattering from the particle is similar to that of a equivalent volume sphere of similar size parameter (see also *Yanamandra-Fisher and Hanner,* 1997; *Xing and Hanner,* 1996).

We also studied the influence of the imaginary refractive index on the phase function. For example, we considered the case of a particle with a real component of refractive index

of 1.75 and varied the imaginary component from 0 - 0.1. (Although the refractive index of NH4SH is not well constrained, the real part of its index of refraction is believed to be about 1.75 at 0.9 μm. See, for example, the discussions of *Bragin, Diem and Guthals* [1977], *Ferraro, Sill and Fink* [1980], and the citations in *Carlson, Lacis and Rossow* [1992].) We find that the phase function does not change very much with the introduction of a modest amount of an imaginary component of the refractive index (over the range of imaginary component of the index of refraction studied) and for the particle size range we used, but, as expected, variation of the real component of the refractive index does affect the phase function.

All of the cases we studied were confined to the study of homogenous particles. For heterogeneous particles the effective refractive index can be simulated by Bruggeman's or Maxwell-Garnett mixing rules for mixed media [see, for example, *Bohren and Huffman*, 1983]. The study of heterogeneous and porous particles by *Yanamandra-Fisher and Hanner* [1997] indicates that the backscatter enhancement can be reduced or even completely suppressed both by a small fraction of contaminants and also by voids equivalent to about 25% of the entire volume of the particle. *Giese et al.* [1978] found a slight enhancement in backscattering to be typical for rough or fluffy absorbing particles, with a range of size parameters (see Eq. 2) equal to 20 to 30.

Although attempts can be made to take the differences in scattering phase functions, discussed above, into consideration, with data from only a small number of sampled angles, the sensitivity of the inversion processes to indices of refraction, particle size distribution parameters, and to differences from particle sphericity, homogeneity, voids, etc. may not be great. Within these and the other severe limitations imposed on instruments for typical exploratory space missions the NEP instrument is, however, suited to providing general characterizations of particle properties.

Using the data measured by our nephelometer instrument we have attempted to define the particle characteristics and cloud properties in the regions traversed by the Probe during

its descent. However, in addition to the described limitations, a number of difficulties have been encountered in these attempts. First, much of the data obtained consisted of very small signals, often within the range of instrumental errors, digitization uncertainties or instrumental noise, so that measurements at the five angles were sometimes hard to compare accurately with each other. Secondly, long after the Galileo Mission launch it was discovered that aerodynamic effects that reordered the particle density, especially in regions near the mirror assembly, might be present during Probe descent, severely affecting the signals measured by the nephelometer. Although considerable effort was made during the instrument design phase to look into aerodynamic effects that might affect the flow' of particles in the sampling volumes, the detailed interaction between the small mirror assembly and the atmosphere was not considered. It was thought that the effects of this cause of particle flow interference would be negligible. However, post flight consideration has shown that these effects may have been especially severe in the 40° and 70° channels, appreciably affecting the signal in the 40° channel, and, perhaps, often reducing the signal in the 70° channel to below the channel sensitivity limits. As noted above, calculations are in progress to estimate the effects of such aerodynamic processes and to attempt to correct the measured data.

Another factor that seriously affected our attempts to interpret the data involved the severe environment experienced by the instrument during descent, including extreme temperatures, rapidly changing temperatures and spatial temperature gradients, all far outside the original instrument specifications. These temperature effects produced uncertainties in the sensitivity corrections and baseline offset corrections to be applied to the data in the temperature regimes outside of our pre-flight calibrations. Following encounter, extensive laboratory tests, attempting to simulate the temperatures and rates of temperature changes encountered during descent, were performed using the spare flight Engineering Unit (EU) nephelometer instrument. The data from these tests were compared with extrapolated pre-flight calibration data for the flight instrument and the Jupiter descent raw

data were corrected using both the extrapolated pre-flight calibrations and the post-encounter spare unit calibrations to establish limits for the corrections to be applied. It proved to be difficult to effectively simulate the baseline variations observed in the flight data, and as a result, we adopted the procedure of normalizing the data to minimum values, discussed above, to analyze the particle characteristics in each of the signal producing regions.

Finally, the actual particles present in the regions in which we obtained signals, as mentioned above, may well be energy-absorbing or non-spherical or non-homogeneous or all of these at once (for example, composed of several allotropes, or "fluffy", with voids, or coated, or containing impurities, etc.). The assumption of spherical homogeneous particles for our model calculations may introduce appreciable discrepancies in attempting to describe these particles.

Inversion of Data to Obtain Particle and Cloud Characteristics. The differential cross sections derived from simultaneous measurements in each of the five scattering channels were compared for best fit with the results obtained from Mie scattering calculations for assumed model particle size distributions. The particles were assumed to be spherical and homogeneous and calculated Mie phase functions were compared with the experimentally measured cross sections to obtain the best fit for the model parameters (mean particle size, r_m, size distribution width, σ, and complex index of refraction, $m_r - im_i$). Because of some of the difficulties cited above, it proved to be possible only to set limits on the values of the parameters, sometimes wide ones. Details of the techniques used in establishing these values are given in the following sections. Work in progress, attempting to obtain applicable particle spatial distributions in the sampling volumes of the nephelometer as a function of descent velocity, ambient atmospheric properties and particle size, and derived corrections to the data in, especially, the 40˚ and 70˚ channels, will enable us to improve the values of these parameters.

Rapid Analytical Technique. A rapid method for attempting to derive the parameters characterizing the particles and cloud properties was employed in the initial data analyses.

Scattering cross sections derived from the observed data were compared with those derived from model calculations as follows:

For the sake of simplicity, the initial analyses of the nephelometer results were carried out using a log-normal distribution of homogeneous spherical particles and Mie theory, which completely characterizes the scattering of light by spheres of a given complex refractive index and size parameter X_{Mie}, where

$$X_{Mie} = 2\pi r/\lambda \tag{2}$$

r is the particle radius and λ is the wavelength of the incoming light (0.904 μm for the Probe nephelometer). For size parameters greater than 2-3, the mean particle size can be determined with considerable accuracy from the width of the diffraction peak.

The particle size distribution function for the model calculations was taken to be a log normal distribution characterized by parameters N_0, r_m, and σ, and defined by the expression

$$n(r, r_m, \sigma) = \frac{C}{r} \exp\left[-0.5 \left(\frac{\ln(r/r_m)}{\ln(\sigma)} \right)^2 \right] \tag{3}$$

$$C = \frac{N_0}{\sqrt{2\pi \ln(\sigma)}} \tag{4}$$

$$N_0 = \int_0^\infty n(r, r_m, \sigma)\, dr \tag{5}$$

where,

$n(r, r_m, \sigma)$ is the number of particles per unit volume with a radius between r and

$r+dr$,

N_0 is the total number of particles per unit volume,

r_m is a mean radius such that half the particles are at r less than r_m,

and,

σ is a width parameter

Angular scattering cross sections for light of wavelength 0.904 µm incident on this distribution were calculated for assumed values of the parameters, N_0, r_m, and σ, assumed values for the index of refraction of the particles, $m = m_r - im_i$, and a Mie scattering calculation program [e.g. see *Bohren and Huffman*, 1983]. The near-Gaussian-shaped angular acceptance function of each of the four forward scatter channels and the measured response of the nephelometer's backscatter channel were also included in these calculations.

The five measured cross section values, $F(5.8^\circ)$, $F(16^\circ)$, $F(40^\circ)$, $F(70^\circ)$, and $F(180^\circ)$, made at scattering angles of 5.8°, 16°, 40°, 70°, and 178° are reduced to four ratios $F(16^\circ)/F(5.8^\circ)$, $F(40^\circ)/F(5.8^\circ)$, $F(70^\circ)/F(5.8^\circ)$, and $F(178^\circ)/F(5.8^\circ)$, for use in comparisons with model calculations to determine the particle size parameters and value of the index of refraction that give the best fit to values for these channel ratios as calculated for a model with these parameters. The selected "best fit" size distribution model is then used with the original five measurements to obtain the total scattering per unit distance, the particle number density and total mass of particles per unit volume.

Sets of nomograms were used as helpful graphical devices for comparing model results and measurements. Conceptually, for a fixed value of m_r, m_i, and σ, we prepared a contour map of the scattering ratio $F(\theta)/F(5.8^\circ)$, laid out on a mesh with the scattering angle ratio as abscissa and the value of r_m as ordinate, typically ranging over a value of 0.1 to 50 µm in 12 logarithmic steps. Actually, only values for the cross section ratios at the measured angles were calculated, and plotted in the form of a nomogram. A set of such nomograms covering a range of the values of m_r, m_i, and σ were prepared. An example of such a nomogram is shown in Figure 8.

The four cross section ratios corresponding to measured data obtained at a fixed time and atmospheric pressure can be located on the nomograms, and in the ideal case the best fit nomogram would show the four measurements on a horizontal line. The elevation of the line would indicate the r_m and the assumed parameters of the nomogram would indicate m_r, m_i and σ. In an actual case a horizontal line is chosen which is the closest to the four points in the sense of a least square fit, and the nomogram is chosen which has the best fit. A computer program can locate the line giving the best fit, but, because the values of cross section ratios along the column for a single angle ratio are at least bivalued in the parametric ranges considered, exhibiting minima and maxima, human intervention may be required to delineate the range of the search. As noted above, an additional problem has been that the measured cross section ratios for $F(40°)/F(5.8°)$ and $F(70°)/F(5.8°)$ have seemed to fall below the expected minima in many cases.

The nomogram method has been used in conjunction with a more methodical computer search in furthering our understanding of the measurements.

More Complete Analyses. For a single particle size and unpolarized light, the Mie scattering phase function as a function of scattering angle $P(\theta)$, the scattering efficiency q_s, and the extinction efficiency q_e depend on three parameters: X_{Mie} and the real and imaginary parts of the refractive index m_r and m_i [e.g. see *Bohren and Huffman*, 1983]. If the wavelength of the incident light is known, as it is in this case, the scattering properties of an ensemble of spherical particles having a log-normal size distribution are given by the complex refractive index $m_r - i\, m_i$, the mean particle radius r_m, the width of the size distribution σ, and the particle number density N_0. The scattering coefficent β_{scat} is a function of N_0, and the cross-section weighted value of q_s:

$$\beta_{scat} = \pi \langle r^2 q_s \rangle N_0 \qquad (6)$$

$$\langle r^2 q_s \rangle = \frac{\displaystyle\int_0^\infty q_s(r) n(r, r_m, \sigma) r^2 dr}{\displaystyle\int_0^\infty n(r, r_m, \sigma) dr} \qquad (7)$$

where $n(r, r_m, \sigma)$ is the log-normal size distribution function defined by Equations 3, 4 and 5.

The differential scattering cross section (the quantity measured by the nephelometer) is given by

$$(N_0 \frac{d\Sigma}{d\Omega})_\theta = \frac{P(\theta) \beta_{scat}}{4\pi} \qquad (8)$$

Fits to the observations were found by minimizing χ^2, the sum of the squared differences of $N_0 d\Sigma/d\Omega$ in all five of the nephelometer channels, with each term in the sum weighted according to the estimated observational error in the corresponding channel.

$$\chi^2 = \sum_{m=1}^{5} \left(\frac{(N_0 d\Sigma/d\Omega)_{obs} - (N_0 d\Sigma/d\Omega)_{Mie}}{E_{obs}} \right)_m^2 \qquad (9)$$

where E_{obs} is the estimated error in each channel.

The dependence of $P(\theta)$ on the Mie scattering parameters X_{Mie}, m_r, and m_i is non-linear, including both quasi-sinusoidal periodicities and sharp resonance spikes. The use of a size distribution with non-zero width smooths out the largest excursions. However, using a standard least squares fitting algorithm involving some form of Newton's method to

obtain a Mie scattering fit to observed values of $N_0 d\Sigma/d\Omega$ often produces results that are difficult to apply without considerable confusion and critical evaluation. Also, the time required to calculate a Mie scattering phase function increases linearly with X_{Mie}, and becomes non-trivial for $X_{Mie} \geq 20$.

For these reasons, the Mie scattering fits to the nephelometer data were carried out by first constructing three-dimensional grids containing the Mie scattering values of the phase function in each channel at regular intervals in three of the free parameters in the set r_m, σ, m_r, and m_i. For each point in the grids, $P(\theta)$ was calculated and convolved with the angular response function of the nephelometer to produce $(N_0 d\Sigma/d\Omega)/\beta_{scat}$ for each of the five instrument channels. Since $N_0 d\Sigma/d\Omega$ has a simple linear dependence on β_{scat}, the optimum value of β_{scat} could be quickly calculated for any location in the grid and any observed $N_0 d\Sigma/d\Omega$, so there was no need to include β_{scat} in the grid itself.

Two such grids were constructed, one in which n_i was held constant at zero, and one in which σ was held constant at 1.5. Although grids could have been constructed using all four parameters at once, practical considerations of file size and search time, including error estimation, mitigated against their preparation.

There is little a priori evidence that the Jovian cloud particles involved in these measurements are absorbing, since the major condensible constituents of Jupiter's atmosphere all have, or are expected to have, very low absorption coefficients at 0.9 μm. (See, for example, the optical constants for NH3 ice given by *Martonchik, Orton and Appleby* [1984], for H2O ice by *Downing and Williams* [1975]. For NH4SH ice, although the optical constants are not well constrained, the discussions of *Bragin, Diem and Guthals* [1977], *Ferraro, Sill and Fink* [1980], and the citations in *Carlson, Lacis and Rossow* [1992] are useful.) This was the rationale for the first grid. Values of $N_0 d\Sigma/d\Omega$ were calculated for $\sigma = (1.2, 1.4, 1.6, 1.8)$, $m_r = (1.20, 1.22, 1.24, \dots 1.70)$, and 80 values of r_m distributed at equal intervals of $\log r_m$ between $X_{Mie} = 3.0$ and $X_{Mie} = 1000$, which means that each successive value of r_m is about 1.075 times the previous value. Fits to the

Nephelometer observations were done by first performing a brute-force search of the entire grid, calculating at each point the value of β_{scat} which would minimize χ^2. The 50 grid points with the lowest χ^2 were recorded, and for each of these the best fit in the immediate vicinity was sought by interpolation on the grid. For the most prominent cloud seen, at a pressure near 1.3 bar, the best fits found for this grid were for particles of 2-5 μm radius and low n_r, but, as mentioned above, even the best fits failed to reproduce the exceedingly low signals observed in the 40° and 70° scattering channels.

As expected [*Ragent et al.*, 1992), the results obtained for non-absorbing particles showed that σ is quite ill-defined by the nephelometer data. Also, in many cases the optimum value of m_r was found to be 1.2, the lower bound of the first grid. So another grid was constructed in which σ was held constant at a value of 1.5, and m_i was varied instead. $N_0 d\Sigma/d\Omega$ was calculated for values of $m_i = $ (0., 10^{-4}, 2×10^{-4}, 4×10^{-4}, 8×10^{-4}, ..., 0.1024). The range of m_r values was also changed to $m_r = $ (1.1, 1.15, 1.2, ... 1.8). Search and interpolation in this grid revealed two discrete solution regions for the cloud at 1.3 bars: 1) m_r in the range 1.7-1.8 (consistent with the little that is known about the optical properties of ammonium hydrosulfide, the most likely condensate at this pressure level), r_m near 1 μm, and m_i near 0.05 (which requires some component with a substantial amount of absorption), and 2) non-absorbing, 7-8 μm particles with $m_r < 1.2$ (which would require some very unusual composition if the cloud particles are homogenous, but might be mimicked by non-spherical "fluffy" particles containing many internal voids). Both these solution regions succeed in reducing the predicted signal in the 40° and 70° channels, while maintaining the observed relationships among the signals in the other three channels.

If the signals in the 40° and 70°channels are assigned zero weight, as might be appropriate if unknown portions of the cloud particles were being systematically swept clear of the sampling volumes in these two channels, then the remaining observations are not enough to unambiguously determine the Mie scattering parameters. Finite volumes in the 3-dimensional grids can fit the data in the remaining three channels perfectly. For a point at

1.24 bars (measurement number 56) in the "NH4SH" cloud, there are two such volumes in the non-absorbing particle grid (recalculated with a lower bound for m_r at 1.1): one centered on a line running from $(r_m, m_r, \sigma, \beta_{scat}) = (0.8\mu m, 1.45, 1.8, 3.2 \times 10^{-4}\ m^{-1})$, Case B1 in Tables Ia, IIa and IIIa, to $(1.1\mu m, 1.44, 1.3, 3.5 \times 10^{-4}\ m^{-1})$, Case B2, and the other centered on a line running from $(r_m, m_r, \sigma, \beta_{scat}) = (2.3\mu m, 1.32, 1.8, 3.8 \times 10^{-4}\ m^{-1})$, Case B3, to $(5.1\mu m, 1.15, 1.2, 3.8 \times 10^{-4}\ m^{-1})$, Case B4. Clouds detected at other points on the probe descent tend to give similar results. Solution sets for three cloud levels for are shown in Table Ia. Cases A1, A2, A3, and A4 at 0.46 bars and Cases C1, C2, C3, and C4 at 3.51 bars are defined as the limits for the lines in the grid on which volumes of points fitting the data are centered, analogous to Cases B1, B2, B3, and B4 at 1.24 bars, the limiting cases described above. The pressures of 0.46, 1.24, and 3.51 bars, correspond to altitudes of 17.0, -5.6, and -39.0 kilometers above the one bar level, or measurement numbers 7, 56, and 115. In Table IIa are listed the derived particle number densities and their total mass per unit volume at these pressures (assuming the cloud particles have the same bulk density as liquid water). Table IIIa lists optical depths, columnar particle number loading, and columnar particle mass loading in the three major cloud structures discussed above, for the particle characteristics at the pressure levels in each structure, as given in Tables Ia and IIa. These Table IIIa quantities were derived by using the ratio of the average 5.8° channel cross section measured in each structure to that of the 5.8° cross section measured at the particular pressure level in that structure listed in Table Ia, to determine the average value for each of the results listed in Tables Ia and IIa, and then multiplying by the altitude extent of the structure. This procedure assumes that the particle properties are uniform throughout the cloud structure considered, as is fairly well justified by the constant ratio among the readings in the various channels over the extent of each region considered, as shown, for example in Figure 6b. Also included in Tables Ib, IIb and IIIb are the special solutions discussed above, labeled B_a and B_b, solutions that

utilized the data from all five channels and the grid with σ fixed at 1.50, and including absorption through the use of the imaginary part of the index of refraction, m_i.

Very similar ranges of solutions are found if the 70° channel is given zero weight and the observed signal in the 40° channel is increased by a factor of 2 for the cases at pressure levels of 1.24 and 3.51 bars (measurement numbers 56 and 115), and to a factor of 5 for cases at a pressure level 0.46 bars (measurement number 7) in attempting to simulate the corrections to the data in this channel that may be obtained from the aerodynamic calculations now in progress.

Because of the uncertainties introduced by the factors mentioned above it was only possible to give rough values or ranges for estimates of particle sizes in Tables I, II and III. We wish to emphasize that the values quoted may contain large uncertainties whose magnitudes are difficult to estimate, and that they should only be used as an indication of the probable particle and cloud characteristics. As a guide to appreciating the difficulties involved in characterizing these sparse particles, we note, by analogy with terrestrial examples, that typical "visibilities" in some of these "thin fog-like" structures at $\lambda = 0.904$ μm may be as large as 10 to 100 kilometers (visibility $= 3.9 / \beta_{scat}$, see *Hinds*, 1982).

In summary, the results from Table III indicate that the total amount of particulate matter directly encountered by the Probe from deployment at about 0.46 bars down to below 10 bars was small. Although it has proved to be difficult to firmly definitize the particle characteristics, the results do tend to bound these characteristics to the ranges shown in Tables I, II and III. Mean particle radii appear to be limited to somewhat less than one to about 5 μm, although particles of radius equal to a few μm often give the best matches. Real indices of refraction are found to lie in the range of about 1.3 to 1.6, assuming that the particles are not highly absorbing, or highly non-spherical, or "fluffy" particles with large voids. NH_3 and H_2O particles are covered by this range, whereas NH_4SH particles are not. If we allow some absorption at our wavelength, 0.904 μm, then the derived values for m_r in the 1.3 bar structure also include values between 1.7 and 1.8, appropriate for

NH4SH. In general, no large particles greater than about 5 μm in radius matched our data, except for the possibility of somewhat larger particles of very low indices of refraction, for example particles containing large void portions. Optical depths in the cloud structures labeled A and C are of the order of 0.1, and between 1 and 2 in the cloud structure B. The peak condensed mass of particles per unit volume was in the range of 1 to 30×10^{-8} kg-m^{-3} in A, about 1 to 4×10^{-8} kg-m^{-3} in C, and about 2 to 12×10^{-7} kg-m^{-3} in cloud B.

In cloud structure C, the suspected "reduced water" cloud, the optical thickness of about 0.1 and the peak density of condensed particles of about 1 to 4×10^{-8} kg-m^{-3} are comparable with the values calculated by *Engel et al.* [personal communication] for the case of assumed water abundance of 0.2 solar and a subsidence velocity of about 1.5 m-sec^{-1}. It should be noted, however, that the values quoted by Engel et al. [personal communication] change very rapidly with subsidence velocity so that almost any reasonable set of experimental values within, say an order of magnitude of those determined in this experiment, can be matched with a small change in subsidence velocity.

5.0 Discussion and Conclusions

Valid nephelometer data were obtained during descent of the Probe in the Jovian atmosphere from deployment at pressures of about 0.46 bars down to pressures somewhat greater than 12 bars, where the instrument ceased to yield reliable measurements. Evidence for at least some extremely small amount of particulate matter in the atmosphere in the vicinity of the Probe was present during much of this portion of the descent trajectory. It should be emphasized that the nephelometer measured scattering from volumes in the near vicinity of the Probe so that local inhomogeneities in the concentration of particles, for example, as "holes" or denser regions in the general particle density configuration, could yield data unrepresentative of the average conditions in a larger sample of the atmosphere. In addition, the magnitudes of even the largest signals obtained during descent were small,

implying that the densest particle concentrations encountered were small, that is, that the atmosphere along the descent trajectory was relatively free of particles and accordingly, that the concentration of condensible species was low. However, some of these low number density particle-bearing regions that exhibited identifiable vertical structures had appreciable vertical extents, for example from five to 10 kilometers, so that quantities such as opacities might still be modestly appreciable.

The small signals, and the inferred small quantities of particulate matter present in this 5μm "hot spot" portion of the Jovian atmosphere are in accord with the results from several of the other Probe experiments [*Niemann et al.*, this issue; *Sromovsky et al.*, this issue; *Seiff et al.*, this issue], as well as from the conclusions that may be drawn from measurements of other 5-μm hot spots by the Galileo Orbiter NIMS, [*R. Carlson et al.*, 1996; *Roos-Serote et al.*, this issue], and from Earth-based [*Orton et al.*, 1996; *Orton et al.*, this issue] and Hubble telescope observations [*Chanover*, 1997; *Chanover et al.*, submitted]. In addition, the general description of the particulates that we inferred from our measurements is in good semi-quantitative agreement with the summary description presented by *West, Strobel and Tomasko* [1986] for the clouds in a 5-μm hotspot .

After passing through the tenuous lower portion of a particle structure assumed to be an ammonia cloud, and encountering a very modest cloud structure based at 1.34 bars, and a very feeble structural feature in the 2 to 4.5 bar region, the Galileo Mission Probe descended in the Jovian atmosphere to depths corresponding to pressures greater than 10 bars without encountering any further appreciable particulate matter. Notwithstanding the very small concentrations of particulate matter observed, the locations of the apparent coherent structures composed of these sparse particles generally appear to validate the presence of condensates in regions roughly in accord with those expected from thermochemical equilibrium considerations using species compositions similar to those predicted to be present from comparisons with the solar composition. The concentrations of these species, in accord with the nephelometer and other Galileo Probe experimental

measurements and inferences from Galileo Orbiter experiments and earth-based measurements dealing with 5μ hot spots, are very small. The tentatively assigned species, and structures associated with the small concentrations of particles composed of these species, include ammonia and an ammonia cloud, and an ammonia plus hydrogen sulfide species, e.g. ammonium hydrosulfide, cloud. Surprisingly, it has proved to be difficult to positively identify the presence of water and an associated water cloud. This species may be, and, probably, is present, but the concentration of particles composed of water is apparently so small that its presence in condensed form was not unambiguously identified. A small extended minor concentration of particles occurred at depths centered at about 3.5 bars in a region that would be suggestive of condensed water except that the low apparent amount of condensation, as indicated by the size of the signals measured, and low vapor pressures measured by other experiments at these altitudes make such a conclusion uncertain at this time. The composition of the condensed species in this region is, thus at present, not positively established, although H_2O is favored. Theoretical suggestions, involving, for example, moderate subsidence, lateral atmospheric mixing motion or other explanations, are now appearing, attempting to explain the apparent reduced species concentration we observed. However, objections to suggested mechanisms for producing downdrafts in hotspots have been raised (see, e.g., *Seiff et al.*, this issue), and none of the current dynamic models for hotspots is yet mature enough to explain the observational data obtained. In any event, no massive cloud structure composed of particles of water or any other species was observed in the region sampled during Probe descent.

Mean particle radius sizes appear to be in the slightly sub-micron to few micron range in the clouds encountered during descent, and, in accord with the measured low particle concentrations and small local volume scattering cross sections, the clouds are characterized by low to modest optical depths and very low mass loadings.

REFERENCES

Ackerman, A. S., O. B. Toon and P. V. Hobbs, Dissipation of marine stratiform clouds and collapse of the marine boundary layer due to depletion of cloud condensation nuclei by clouds, *Science, 262*, 226-229, 1993.

Atreya, S. K. and P. N. Romani in *Planetary Meteorology* , edited by G. E. Hunt, Cambridge Univ. Press, Cambridge, 17-68, 1985.

Atreya, S. K., *Atmospheres and Ionospheres of the Outer Planets and Their Satellites*, Springer-Verlag, New York and Berlin, 1986.

Atreya, S. K., M. H. Wong, T. Owen, H. Niemann and P. Mahaffy, Chemistry and clouds of the atmosphere of Jupiter: a Galileo perspective, in *Three Galileos: The Man, The Spacecraft, The Telescope*, edited by J. Rahe, C. Barbieri, T. Johnson and A. Sohus, Kluwer Academic Publishers, Dordrecht, 1997.

Baker, R. D. and G. Schubert, Jovian hotspots and convective entrainment, Supplement to Eos, *Transactions, AGU, 78*, F414, 1997.

Banfield, D. J., M. Bell, P. J. Gierasch, E. A. Ustinov, A. Vasavada, A. P. Ingersoll, M. J. S. Belton, and the Galileo Imaging Team, Jupiter cloud structure from Galileo images: Local cloud systems, *Bull. Amer. Astron. Soc. 29*, 1007, 1997.

Bézard, B., J.-P. Baluteau, and A. Marten, Study of the deep cloud structure in the equatorial region of Jupiter from Voyager infrared and visible data, *Icarus 54*, 434-455,

1983.

Bohren, C. F. and D. R. Huffman, *Absorption and Scattering of Light by Small Particles*, John Wiley and Sons, New York, 1983.

Bjoraker, G., The gas composition and vertical cloud structure of Jupiter's troposphere derived from five-micron spectroscopic observations. Ph.D. dissertation, Department of Planetary Sciences, University of Arizona, Tucson, 1985.

Bjoraker, G. L, H. P. Larson, and V. G. Kunde, The abundance and distribution of water vapor in Jupiter's atmosphere, *Astrophys.,J., 311*, 1058-1072, 1986.

Bragin, J., M. Diem, and D. Guthals, The vibrational spectrum and lattice dynamics of polycrystalline ammonium hydrosulfide, *J. Chem Phys., 67*, 1247-1256, 1977.

Carlson, B. E., W. B. Rossow, and S. G. Orton, Cloud microphysics of the giant planets, *J. Atmospheric Sci., 45*, 2055-2081, 1988.

Carlson, B. E. A. A. Lacis, and W. B. Rossow, The abundance and distribution of water vapor in the Jovian troposphere as inferred from Voyager IRIS observations, *Astrophys. J., 388*, 648-668, 1992.

Carlson, B. E. A. A. Lacis, and W. B. Rossow, Tropospheric gas composition and cloud structure of the Jovian North Equatorial Belt, *J. Geophys. Res. 98*, 5251 - 5290, 1993.

Carlson, R., W. Smythe, K. Baines, E. Barbinis, K. Becker, R. Burns, S. Calcutt, W. Calvin, R. Clark, G. Danielson, A. Davies, P. Drossart, T. Encrenaz, F. Fanale, J.

Granathan, G. Hansen, P. Herrera, C. Hibbitts, J. Hui, P. Irwin, T. Johnson, L. Kamp, H. Kieffer, F. Leader, E. Lellouch, R. Lopes-Gautier, D. Matson, T. McCord, R. Mehlman, A. Ocampo, G. Orton, M. Roos-Serote, M. Segura, J. Shirley, L. Soderbloom, A. Stevenson, F. Taylor, J. Torson, A. Weir and P. Weissman, Near infrared spectroscopy and spectral mapping of Jupiter and the Galilean satellites: Results from Galileo's initial orbit, *Science 274*, 385-388,1996.

Chanover, N., Vertical structure of Jupiter's atmosphere and the Galileo Probe entry latitude, *Bull. Amer. Astron. Soc. 29*, 1006, 1997.

Chanover, N., D. Kuehn, and R. F. Beebe, Vertical structure of Jupiter's atmosphere at the Galileo Probe entry latitude, *Icarus*, submitted.

Clapp, M. L. and R. E. Miller, Shape effects in the infrared spectrum of ammonia aerosols, *Icarus, 105*, 529-536, 1993

Collard, A. D., L. A. Sromovsky, G. L. Bjoraker and G. S. Orton, The deep water abundance from remote and in situ observations, *Bull. Amer. Astron. Soc. 92*, 1006, 1997.

de Pater, I. and D. L. Mitchell, Radio observations of the planets: the importance of laboratory measurements, *J. Geophys. Res., 98*, 5471-5490, 1993

Del Genio, A. D, Moist convection and the vertical structure and water abundance of Jupiter's atmosphere, *Icarus 84*, 29-53, 1990.

Downing, H. D. and D. Williams, Optical constsnts of water in the infrared, *J. Geophys. Res., 80,* 1656-1661, 1975.

Draine, B. T., The discrete dipole approximation and its application to interstellar graphite grains, *Astrophys. J., 333,* 848-872, 1988.

Draine, B. T. and P. J. Flatau, Discrete dipole approximation for scattering calculations, *J. O. S. A., 11,* 1491-1499, 1994.

Ferraro, J. R., G. Sill, and U. Fink, Infrared intensity measurements of cryodeposited thin films of NH3, NH4SH, H2S and assignments of absorption bands, *App. Spectr., 34,* 525-533, 1980.

Folkner, W. M. and R. Woo, Ammonia abundance at the Galileo Probe site derived from absorption of its radio signal, this issue.

Gierasch, P. J., B. J. Conrath, and J. A. Magalhaes, Zonal mean properties of Jupiter's upper troposphere from Voyager infrared observations, *Icarus 67,* 456 - 483, 1986.

Giese, R. H., K. Weiss, R. H. Zerull and T. Ono, Large fluffy particles: a possible explanation of the optical properties of interplanetary dust, *Astron. Astrophys., 65,* 265-272, 1978.

Goodman, J. J., B. T. Draine and P. J. Flatau, Application of fast-Fourier transform techniques to the discrete dipole approximation, *Opt. Lett., 16,* 1198-1200, 1990.

Hinds, W. C., *Aerosol Technology,* John Wiley and Sons, New York, 1982

Irwin, P. G. J., A. L. Weir, S. Smith, F. W. Taylor, A. L. Lambert, S. Calcutt, R. Carlson, K. Baines, P. Drossart, Th. Encrenaz, and M. Roos-Serote, Cloud structure and composition of Jupiter retrieved from Galileo NIMS real-time spectra, this issue.

Larson, H. P., D. S. Davis, R. Hoffman and G. Bjoraker, The Jovian atmospheric window at 2.7 μm: a search for H_2S, *Icarus, 60*, 621-639, 1984.

Lewis, J. S. and R. G. Prinn, *Planets and their Atmospheres: Origin and Evolution*, Academic Press, New York, 1984.

Magalhaes, J. A., A. L. Weir, P. J. Gierasch, B. J. Conrath, S. S. Leroy, Zonal motion and structure in Jupiter's upper troposphere from Voyager infrared and imaging observations, *Icarus , 80*, 39-72, 1990.

Marten, A., D. Rouen, J.-P. Baluteau, D. Gautier, B. Conrath, R. Hanel, V. Kunde, R. Samuelson, A. Chedin and N. Scott, Study of the ammonia ice cloud layer in the equatorial region of Jupiter from the infrared interferometric instrument on Voyager, *Icarus , 46*, 233 - 248, 1981.

Martonchik, J. V., G. S. Orton and J. F. Appleby, Optical properties of NH_3 ice from the far infrared to the near ultraviolet, *Appl. Opt.*, 23, 541-547, 1984.

Mischenko, M. I., Light scattering by size/shape distributions of randomly oriented axially symmetric particles of a size comparable to a wavelength, *Appl. Opt., 32*, 4652-4666, 1993.

Mishchenko, M. I., and L. D. Travis, Light scattering by polydispersions of randomly oriented spheroids with sizes comparable to wavelengths of observation, *Appl. Opt,* *33*, 7206-7225, 1994.

Mischenko, M. I., L. D. Travis, R. A. Kahn and R. A. West, Modeling phase functions for dustlike tropospheric aerosols using a shape mixture of randomly oriented polydisperse spheroids, *J. Geophys. Res., 102*, 16,831-16,847, 1997.

Niemann H. B., S. K. Atreya, G. R. Carignan, T. M. Donahue, J. Haberman, D. Harpold,
R. E. Hartle, D. M. Hunten, W. Kasprzak, P. Mahaffy, T. C. Owen and S. Way, The composition of the Jovian atmosphere as determined by the Galileo Probe mass spectromenter, this issue.

Orton, G. S. and R. Terrile, Multiple-frequency sounding of a Jovian cloud *Icarus* , *35*, 297-307, 1978.

Orton, G. S., J. F. Appleby, and J. V. Martonchik, The effect of ammonia ice on the outgoing thermal radiance from the atmosphere of Jupiter, *Icarus* , *52*, 94 - 116, 1982.

Orton, G., J. L. Ortiz, K. Baines, G. Bjoraker, U. Carsenty, F. Colas, D. Deming, P. Drossart, E. Frappa, J. Friedson, J. Goguen, W. Golisch, D. Griep, C. Hernandez, W. Hoffmann, D. Jennings, C. Kaminski, J. Kuhn, P. Laques, S. Limaye, H. Lin, J. Lecacheux, T. Martin, G.McCabe, T. Momary, D. Parker, R. Puetter, M. Ressler, G. Reyes, P. Sada, J. Spencer, J. Spitale, S. Stewart, J. Varsik, J. Warell, W. Wild, P. Yanamandra-Fisher, A. Dayal, L. Deutsch, G. Fazio, and J. Hora, Results of earth-based observations of the Galileo Probe entry site, *Science* , *272*, 839 - 840, 1996.

Orton, G. S., B. M. Fisher, S. T. Stewart, J. L. Ortiz, M. Marinova, S. Hinkley, V. Krishnan, M. Masanovic, J. Tesic and A. Tziolas, Characteristics of the Galileo Probe entry site from Earth-based remote sensing observations, this issue.

Pollack, J. B.., and J. N. Cuzzi, Scattering by nonspherical particles of size comparable to a wavelength: a new semi-empirical theory and its application to tropospheric aerosols, *J. Atmos. Sci., 37,* 868, 1980.

Pritchard, B. S. and Elliott, W. G., Two instruments for atmospheric optics measurements, *J. O. S. A., 50,* 191-202, 1960.

Purcell, E. M. and C. R. Pennypacker, Scattering and absorption of light by nonspherical dielectric grains, *Astrophys. J., 186,* 705-714, 1977.

Ragent B., C. A. Privette, P. Avrin, J. G. Waring, C. E. Carlston, T. C. D. Knight and J. P. Martin, Galileo Probe nephelometer experiment, *Space Science Reviews, 60,* 179-201, 1992.

Ragent B., D. S. Colburn, P. Avrin and K. A. Rages, Results of the Galileo probe nephelometer experiment, *Science, 272,* 854-856, 1996.

Roos-Serote, M. P. Drossart, Th. Encrenaz, R. W. Carlson, K. H. Baines, F. W. Taylor. The analysis of 5 μm hot spots from Galileo/NIMS spectra: Results for cloud opacity, water and ammonia, *Bull. Amer. Astron. Soc.,29,* 1005, 1997.

Roos-Serote, M. P. Drossart, Th. Encrenaz, E. Lellouch, R. W. Carlson, K. H. Baines, L.

Kamp, R. Mehlman, G. S. Orton, S. Calcutt, P. Irwin, F. Taylor and A. Weir, Analysis of Jupiter NEB hot spots in the 4-5 µm range from Galileo/NIMS observations; measurements of cloud opacity, water and ammonia, this issue.

Schuerman, D. W., (editor), *Light Scattering by Irregularly Shaped Particles.*, Plenum, New York, 1980.

Schuerman, D. W., R. T. Wang, B. A. S. Gustafson, and R. W. Schaefer, 1981: Systematic studies of light scattering. 1. Particle shape, *Appl. Optics*, *20*, 4039-4050, 1981.

Seiff, A., D. B. Kirk, T. C. D. Knight, R. E. Knight, J. D. Mihalov, L. A. Young, F. S. Milos, G. Schubert, R. C. Blanchard and D. Atkinson, Thermal structure of Jupiter's atmosphere near the edge of a 5-micron hot spot in the northern equatorial belt, this issue.

Showman, A. P. and A. P. Ingersoll, Dynamical implications of Galileo Probe data, Supplement to Eos, *Transactions, AGU, 78*, F413, 1997.

Showman, A. P. and A. P. Ingersoll, Interpretation of Galileo Probe data and implications for Jupiter's dry downdrafts, submitted to *Icarus*.

Smith, P. H. and M. G. Tomasko, Photometry and polarimetry of Jupiter at large phase angles. II. Polarimetry of the South Tropical Zone, South Equatorial Belt and the polar regions from the pioneer 10 and 11 missions, *Icarus*, *58*, 35 - 73, 1984.

Sromovsky, L. A., A. D. Collard, P. M. Fry, G. S. Orton, M. T. Lemmon, M. G. Tomasko and R. S. Freedman, Galileo Probe measurements of thermal and solar radiation fluxes in the Jovian atmosphere, this issue.

Stewart, S. and G. Orton, The cloud structure and morphology of Jovian equatorial hot

spots, *Bull. Amer. Astron. Soc.*, *29*, 1006, 1997.

Stewart, S., G. S. Orton, B. M. Fisher and K. H. Baines, The cloud structure of the Jovian

north equatorial zone: context of the Galileo Probe entry latitude, this issue.

von Zahn, D. M. Hunten and G. Lehmacher, The helium mass fraction in Jupiter's

atmosphere found to match that in the Sun's convective zone, this issue.

Weidenschilling, S. J. and J. S. Lewis, Atmospheric and cloud strcutre of the Jovian

planets, *Icarus 20*, 465-476, 1973.

Weir, A. L., P. G. J. Irwin, S. Smith, F. W. Taylor, A. Lambert, P. J. Smith, R. Carlson,

K. Baines. Th. Encrenaz, P. Drossart, and M. Roos-Serote, Jovian atmospheric

structure as revealed by Galileo NIMS, *Bull. Amer. Astron. Soc. 29*, 1005, 1997.

West, R. A., P. N. Kupferman, and H. Hart, Voyager 1 imaging and IRIS observations of

Jovian methane absorption and thermal emission: Implications for cloud structure, *Icarus* ,

61, 311-342, 1985.

West, R. A., D. F. Strobel, and M. G. Tomasko, Clouds, aerosols, and photochemistry

in the Jovian atmosphere, *Icarus 65*, 161-217, 1986.

West, R. A., M. G. Tomasko and L. R. Doose, Optical properties of small mineral dust

particles at visible/near-IR wavelengths: Numerical calculation and laboratory

measurement, pp. 341-343, in *Proceedings of the Eighth Conference on Atmospheric Radiation*, Amer. Met. Soc. 1994.

West, R. A., L. R. Doose, A. M. Eibl, M. G. Tomasko and M. I. Mischenko, Laboratory measurements of mineral dust scattering phase function and linear polarization, *J. Geophs.Res.*, *102*, 16,871-16,881, 1997

Xing, Z. and M. S. Hanner, Light scattering by aggregate particles, *Astron. Astrophys., Main Journal*, in press.

Yanamandra-Fisher, P. V. and M. S. Hanner, Optical properties of non-spherical particles of size comparable to the wavelength of light: Application to comet dust, submitted for publication.

Young, R. E., The Galileo Probe mission to Jupiter: science overview, this issue.

Zerull, R. and R. H. Giese, Microwave analog studies, in *Planets, Stars, and Nebulae, Studied with Polarimetry*, T. Gehrells, Ed., U. Arizona Press, Tucson, 901, 1974.

Zerull, R. H., B. A. S. Gustafson, K. Schulz, and E. Thiele-Corbach, Scattering by aggregates with and without an absorbing mantle: microwave analog experiments, *Appl. Optics*, *32*, 4088-4100, 1993.

FIGURE CAPTIONS

1. Temperatures recorded by the forward scatter source and backward scatter channel source temperature sensors, and the electronics unit internal temperature, all as a function of atmospheric pressure during the Probe descent. The ambient atmospheric temperature is also plotted. Note that starting at about 6 bars, the source temperatures, displaced by about 20° C, follow the ambient atmospheric temperature.

2. Forward scatter source, backward scatter source and contamination (alignment) source monitor readings versus atmospheric pressure during Probe descent.

3. Contamination and alignment channel readings versus pressure during Probe descent.

4. Plots of recorded raw scatter channel readings as a function of ambient atmospheric pressure during the Probe descent.

5. Expanded plots of recorded raw scatter channel readings as a function of ambient atmospheric pressure during the Probe descent. (a) Pressure range of 0.42 to 0.58 bars. (b) Pressure range from 0.7 to 1.8 bars. (c) Pressure range from 1.0 to 1.9 bars. (d) Pressure range from 1.9 to 4.5 bars.

6. Plots of channel cross sections, $F(\theta) = N_0 (d\Sigma/d\Omega)_\theta$ $m^{-1} sr^{-1}$, versus ambient atmospheric pressure, where N_0 is the density of particles and $d\Sigma$ is the differential scattering cross section for scattering from the incident beam into solid angle element $d\Omega$ at scattering angle θ. Error bars (see text) for every other data point are included in Figures 6b and 6c. (a) Pressure range of 0.42 to 0.58 bars. All cross sections

normalized to zero at p = 0.510 bars. Multiplication factors of 1.00, 3.93, 63.17, 58.72, and 27.08 used for 5.8˚, 16˚, 40˚, 70˚ and 178˚ channel cross sections, respectively. (b) Pressure range from 0.7 to 1.8 bars. All cross sections normalized to zero at p = 1.345 bars. Multiplication factors of 1.00, 6.11, 95.0, and 82.5 used for 5.8˚, 16˚, 40˚, and 178˚ channel cross sections, respectively. (c and d) Pressure range from 1.9 to 4.5 bars. All cross sections normalized to zero at p = 3.603 bars. Multiplication factors of 1.00, 7.67, and 30.4 used for 5.8˚, 16˚, and 178˚ channel cross sections, respectively.

7. Scattering phase functions versus scatter angle for a sphere, brick, tetrahedron, cylinder and hexagonal prism. Index of refraction, $n = 1.75$, wavelength, $\lambda = 0.904$ μm, and effective size parameter, $x = 2\pi r/\lambda = 2.7$, where r is the spherical equivalent volume radius. Brick edges are in the ratio 3: 2: 1, the tetrahedron has four equilateral triangle faces, the cylinder height: radius is ~3: 1 , and the hexagonal prism has edges with the ratio of ~3: 1 (the 3 edge is parallel to the six-fold symmetry axis and the 1 edge is perpendicular to it and equal to one half of the distance between vertices of the hexagon).

8. Example of a nomogram showing the values of the ratio $F(\theta)/F(5.8)$ at the other four scattering channel angles of $\theta = 16˚$, 40˚, 70˚ and 178˚ for values of r_m varying from 0.1 μm to 100 μm. For this nomogram calculations of $F(\theta)/F(5.8)$ were performed for spherical particles, a log-normal particle size distribution, and values of $m = m_r - m_i = 1.45$ and $\sigma = 1.50$. A collection of spherical particles distributed in size in a log-normal distribution with values of m and σ used for this nomogram will produce scattering data that will lie on a horizontal line corresponding to a value for r_m. An incident light wavelength of 0.904 μm was used for these calculations.

Table Ia. Solution Sets for Nephelometer Data at a Given Pressure Using Data from 5.8°, 16°, and 178° Channels, $\lambda = 0.904$ μm and $m_i = 0$. (See text.)

Case	Press, bars	r_m, μm	m_r	σ	β_{scat}, $m^{-1} = \beta_{ext}$, m^{-1}
A1 to A2	0.46	0.5 to 0.9	1.53 to 1.49	1.8 to 1.3	$(2.9 \text{ to } 2.9) \times 10^{-5}$
A3 to A4	0.46	4.3 to 5.1	1.38 to 1.38	1.8 to 1.4	$(4.5 \text{ to } 4.5) \times 10^{-5}$
B1 to B2	1.24	0.8 to 1.1	1.45 to 1.44	1.8 to 1.3	$(3.2 \text{ to } 3.5) \times 10^{-4}$
B3 to B4	1.24	2.3 to 5.1	1.32 to 1.15	1.8 to 1.2	$(3.8 \text{ to } 3.8) \times 10^{-4}$
C1 to C2	3.51	1.0 to 1.4	1.54 to 1.49	1.8 to 1.2	$(9.9 \text{ to } 9.0) \times 10^{-6}$
C3 to C4	3.51	2.0 to 3.7	1.49 to 1.56	1.8 to 1.2	$(1.2 \text{ to } 1.4) \times 10^{-5}$

Table Ib. Solution Sets for Nephelometer Data at a Given Pressure Using Data from All Five Channels and $\lambda = 0.904$ μm. (See text.)

Case	Press, bars	r_m, μm	m_r	m_i	σ	β_{ext}, m^{-1}
B_a	1.22	7.9	1.12	0.00	1.50	3.6×10^{-4}
B_b	1.22	0.81	1.76	0.051	1.50	2.4×10^{-4}

Table IIa. Number and Mass Densities from Results in Table Ia

(Assumed Particle Bulk Density $= 10^3$ kg-m^{-3}).

Case	Press, bars	$r_m, \mu m$	σ	$<r^3>, (\mu m^3)$	N, m^{-3}	$\rho, kg\text{-}m^{-3}$
A1 to A2	0.46	0.5 to 0.9	1.8 to 1.3	0.49 to 1.00	$(7.5 \text{ to } 3.8)\times10^{+6}$	$(1.5 \text{ to } 1.6)\times10^{-8}$
A3 to A4	0.46	4.3 to 5.1	1.8 to 1.4	360 to 220.	$(1.9 \text{ to } 2.0)\times10^{+5}$	$(2.9 \text{ to } 1.8)\times10^{-7}$
B1 to B2	1.24	0.8 to 1.1	1.8 to 1.3	2.2 to 1.8	$(3.4 \text{ to } 3.3)\times10^{+7}$	$(3.1 \text{ to } 2.5)\times10^{-7}$
B3 to B4	1.24	2.3 to 5.1	1.8 to 1.2	57 to 150	$(5.2 \text{ to } 1.9)\times10^{+6}$	$(1.2 \text{ to } 1.2)\times10^{-6}$
C1 to C2	3.51	1.0 to 1.4	1.8 to 1.2	4.3 to 3.0	$(7.0 \text{ to } 5.4)\times10^{+5}$	$(1.2 \text{ to } .68)\times10^{-8}$
C3 to C4	3.51	2.0 to 3.7	1.8 to 1.2	38 to 57	$(2.2 \text{ to } 1.4)\times10^{+5}$	$(3.5 \text{ to } 3.3)\times10^{-8}$

Table IIb. Number and Mass Densities from Results in Table Ib

(Assumed Particle Bulk Density $= 10^3$ kg-m^{-3}).

Case	Press, bars	$r_m, \mu m$	σ	$<r^3>, (\mu m^3)$	N, m^{-3}	$\rho, kg\text{-}m^{-3}$
B_a	1.22	7.9	1.50	1030.3	$6.3 \times10^{+5}$	2.7×10^{-6}
B_b	1.22	0.81	1.50	1.12	$3.4 \times10^{+7}$	1.6×10^{-7}

Table IIIa. Optical Depths, Column Particle Number Loading and Column Particle Mass Loading

in Jupiter Clouds Encountered by the Galileo Mission Probe

(from Tables Ia and IIa).

Case	Pressure Range, bars	Optical Depth @ $\lambda = 0.904 \ \mu m$	Particle No. Loading, m^{-2}	Particle Mass Loading, $kg\text{-}m^{-2}$
A1 to A2	0.46-0.53	0.06 to 0.06	$(1.48 \text{ to } .752) \times 10^{10}$	$(2.97 \text{ to } 3.17) \times 10^{-5}$
A3 to A4	0.46-0.53	0.09 to 0.09	$(3.76 \text{ to } 3.96) \times 10^{8}$	$(5.74 \text{ to } 3.56) \times 10^{-4}$
B1 to B2	1.00-1.34	1.5 to 1.6	$(1.58 \text{ to } 1.53) \times 10^{11}$	$(1.44 \text{ to } 1.16) \times 10^{-3}$
B3 to B4	1.00-1.34	1.8 to 1.8	$(2.41 \text{ to } .880) \times 10^{10}$	$(5.56 \text{ to } 5.56) \times 10^{-3}$
C1 to C2	2.45-3.58	0.09 to 0.08	$(6.43 \text{ to } 4.96) \times 10^{9}$	$(1.10 \text{ to } 0.63) \times 10^{-4}$
C3 to C4	2.45-3.58	0.11 to 0.13	$(2.02 \text{ to } 1.28) \times 10^{9}$	$(3.22 \text{ to } 3.03) \times 10^{-4}$

Table IIIb. Optical Depths, Column Particle Number Loading and Column Particle Mass Loading

in Jupiter Clouds Encountered by the Galileo Mission Probe

(from Tables Ib and IIb).

Case Range, bars	Pressure Depth @	Optical Loading, m^{-2} $\lambda = 0.904\ \mu$	Particle No. Loading, $kg\text{-}m^{-2}$	Particle Mass
B_a	1.00-1.34	1.7	2.98×10^9	1.28×10^{-2}
B_b	1.00-1.34	1.1	1.61×10^{11}	7.57×10^{-4}

Cloud Region A. Particulate structure encountered in the pressure range of 0.459 bars to 0.525 bars (altitude range from 17.26 to 14.6 km above the one bar level, measurement numbers 6 to 14), baseline normalized to zero at 0.525 bars.

Cloud Region B. Particulate structure encountered in the pressure range of 1.003 bars to 1.342 bars (altitude range from -0.13 to -7.85 km above the one bar level, measurement numbers 46 to 60), baseline normalized to zero at 1.342 bars.

Cloud Region C. Particulate structure encountered in the pressure range of 2.448 bars to 3.583 bars (altitude range from -26.23 to -39.83 km above the one bar level, measurement numbers 90 to 117), baseline normalized to zero at 3.583 bars.
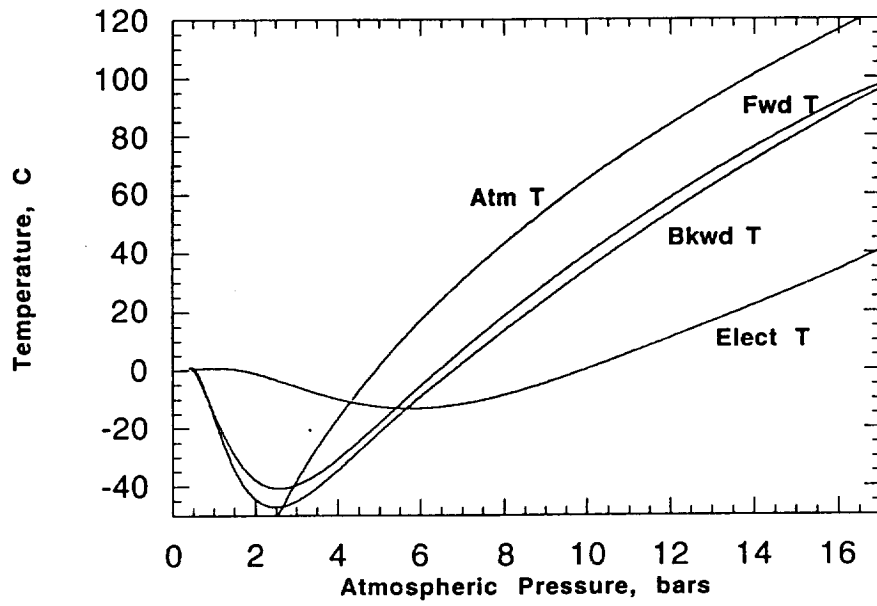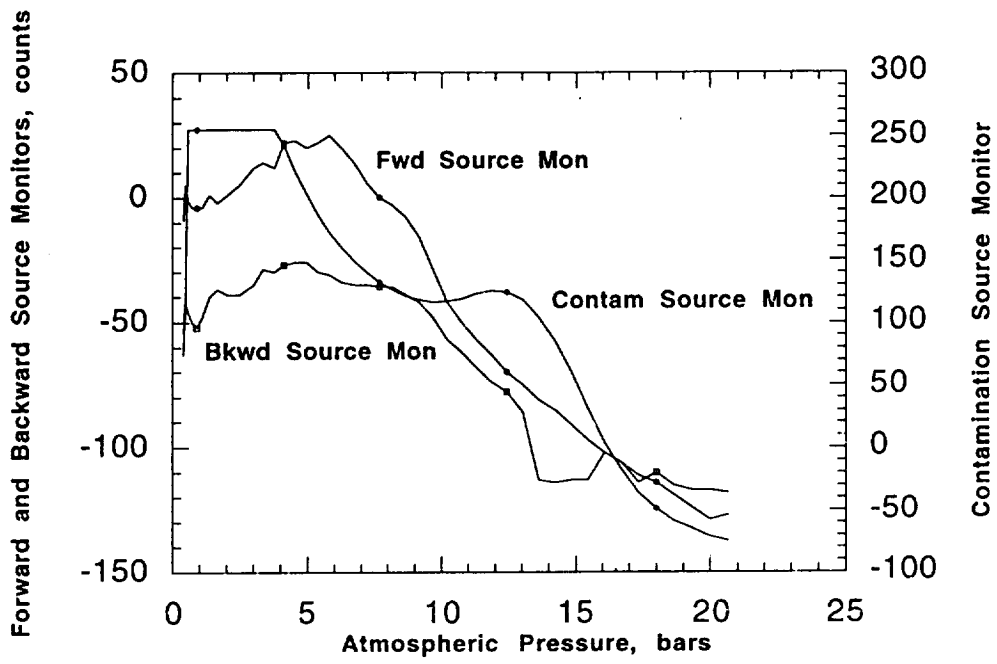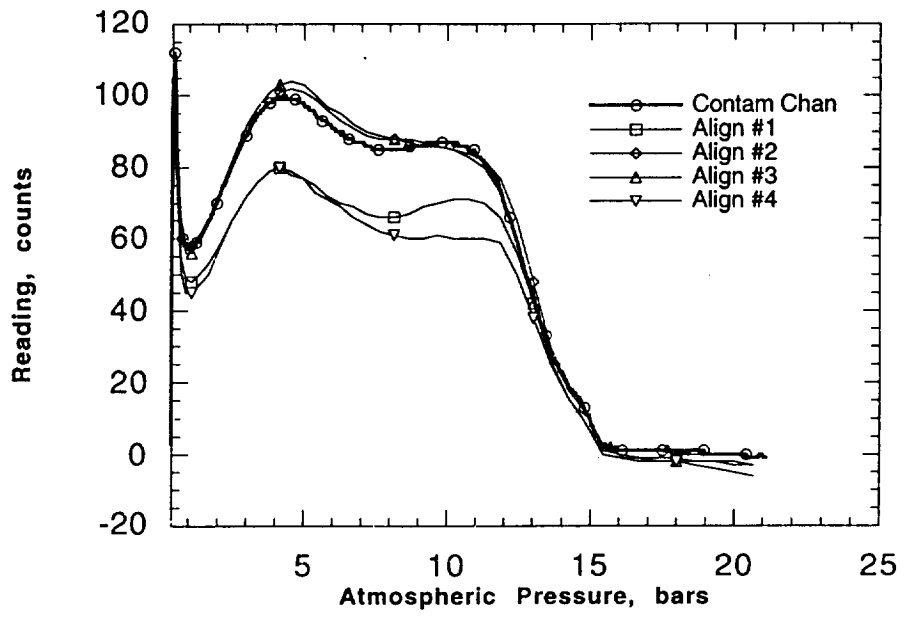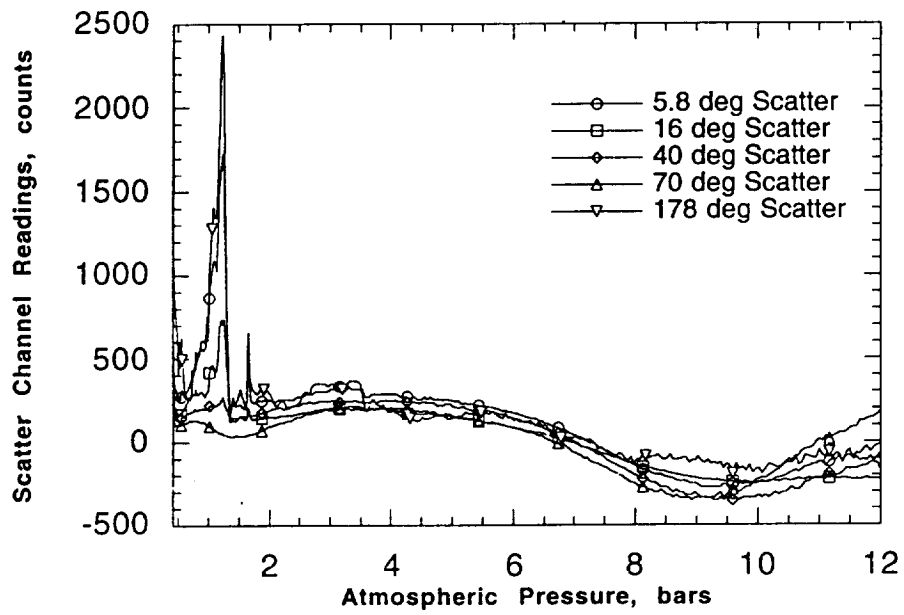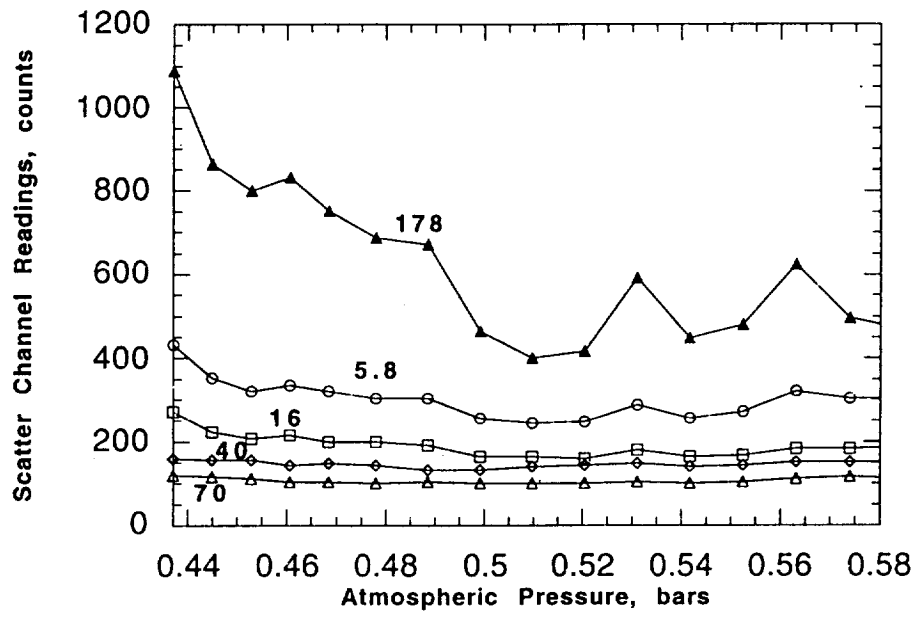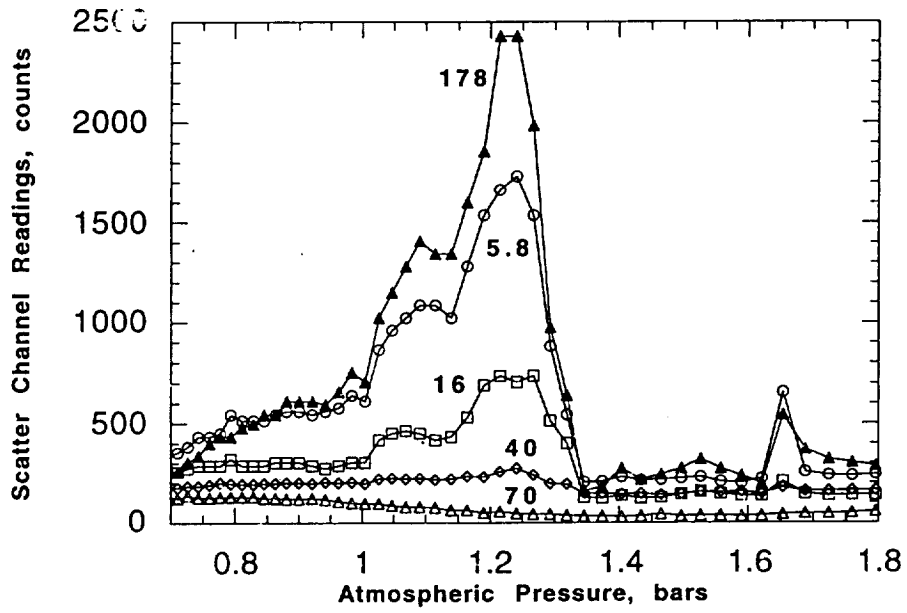
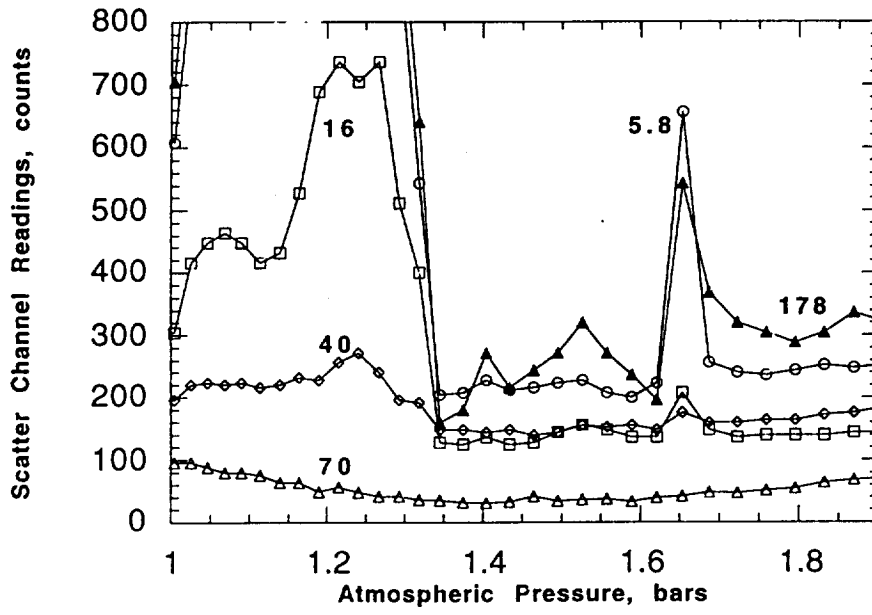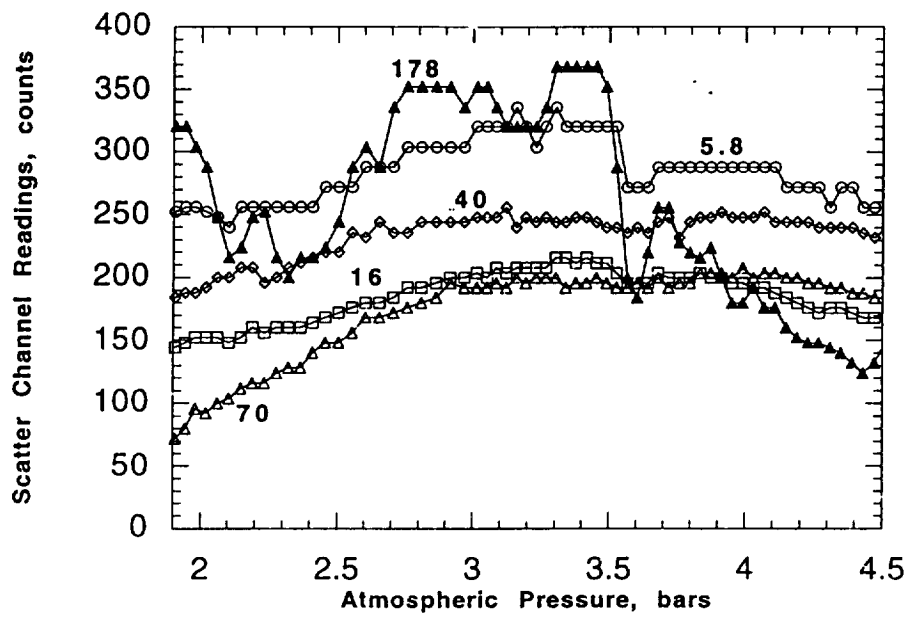Figure 1

Figure 2
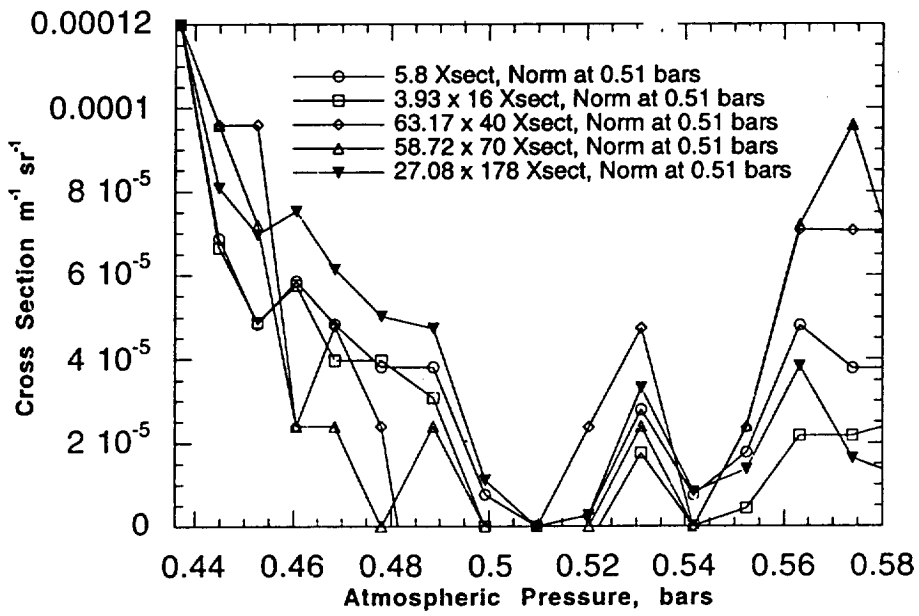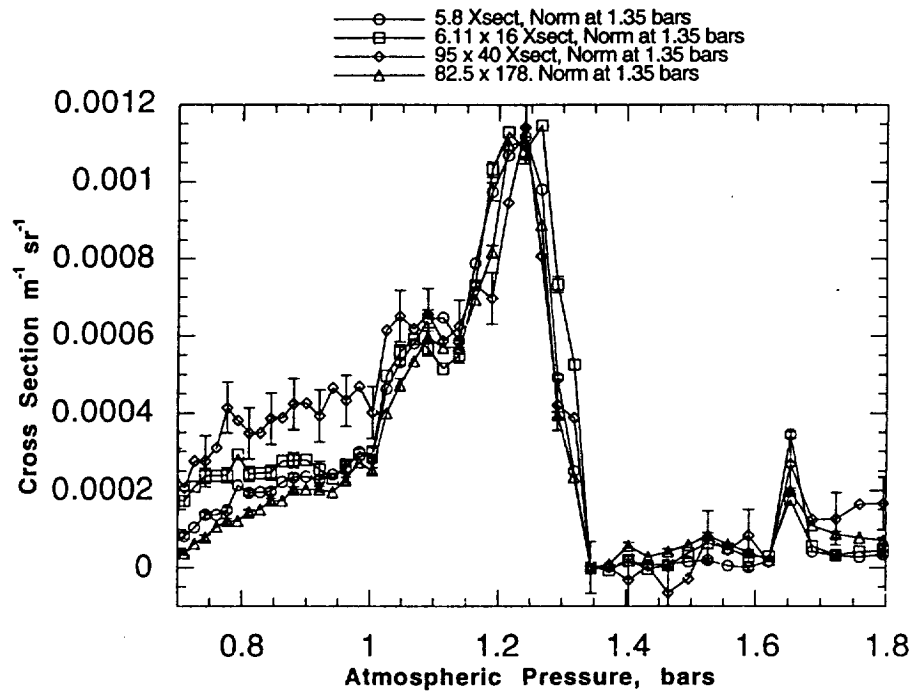
Figure 3

Figure 4

Figure 5a

Figure 5b

Figure 5c

Figure 5d

Figure 6a

Figure 6b
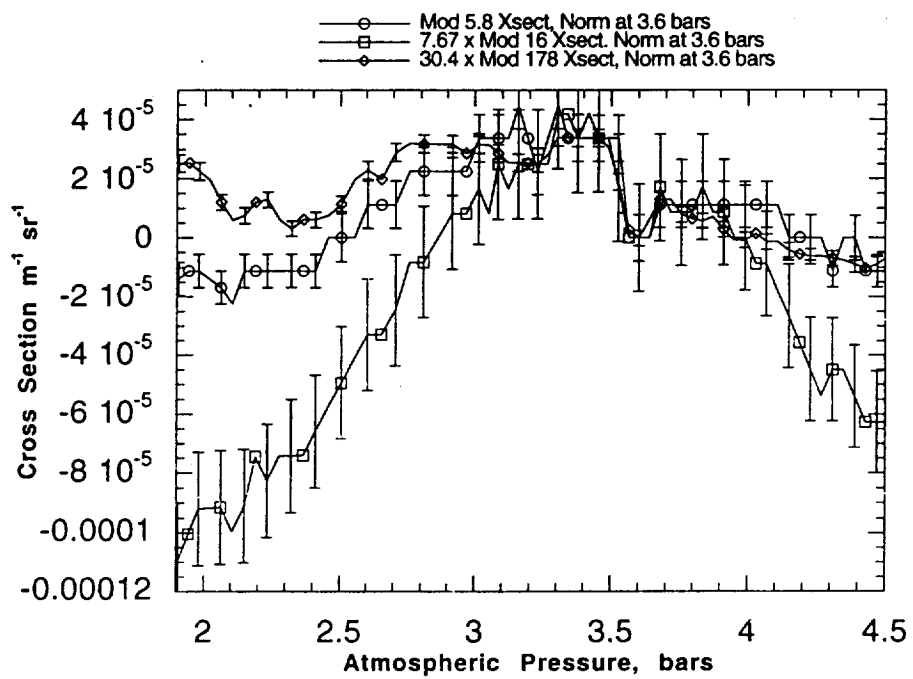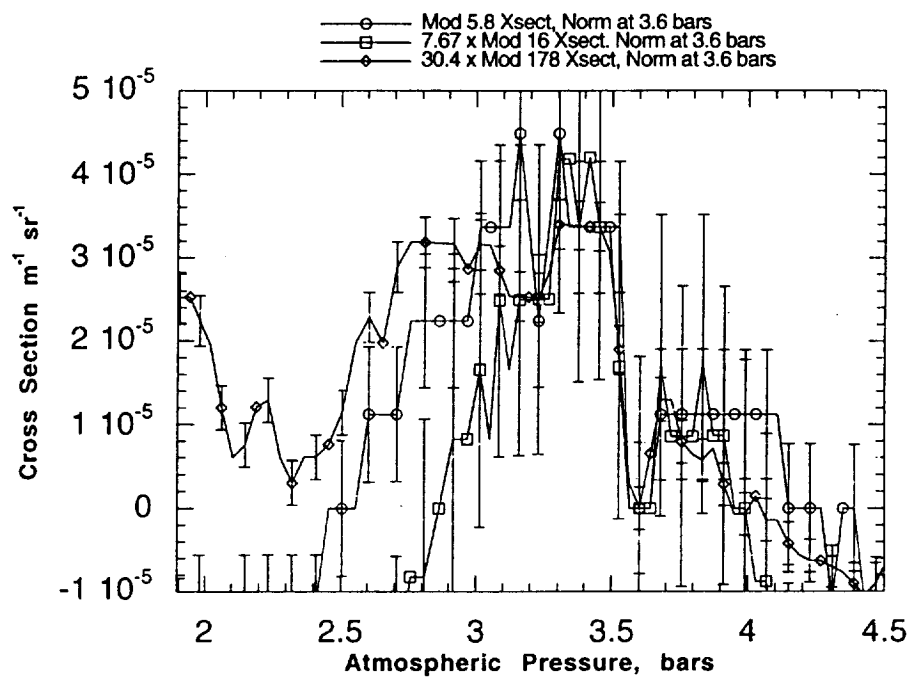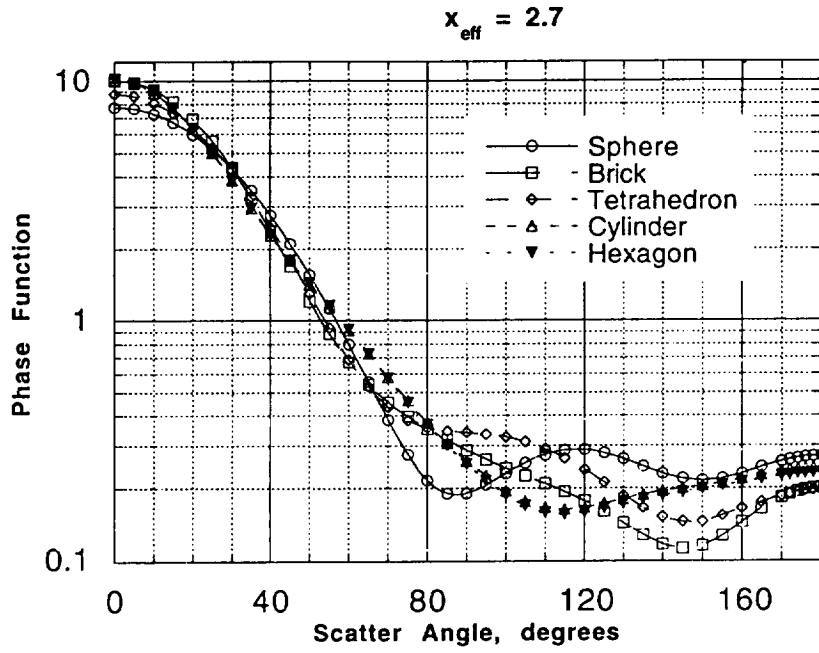
Figure 6c

Figure 6d

$$x_{eff} = 2.7$$

Figure 7

100.0

50.0 ⌐0.585 ⌐0.199 ⌐0.0278 0.14 ⌐0.136

⌐0.534 0.18 ⌐0.181 ⌐0.0258 ⌐0.155
0.50
0.16 0.024⌐ ⌐0.0232 ⌐0.153
20.0 ⌐0.453 0.14 0.14
0.40 ⌐0.153
0.36 0.12 0.020⌐ 0.12
0.018⌐0.0174
10.0 0.32 ⌐0.326 0.10 ⌐0.103 ⌐0.110
0.28 0.09 0.016⌐ 0.10
0.08 0.09
0.24 0.08
5.0 ⌐0.225 0.07 ⌐0.071 0.014⌐0.0141 0.07 ⌐0.072
0.20 0.06 0.012⌐ 0.06
0.18 0.05 0.010⌐ 0.05
0.16 0.04 0.04
0.14 0.036⌐0.0364 0.008⌐0.0075 0.024⌐0.0234
0.12 ⌐0.126 0.032 0.007⌐ 0.020
0.10 0.028 0.006⌐ 0.016
0.024 0.012⌐0.0114
2.0 0.09 ⌐0.086 0.024 ⌐0.0225 0.006⌐0.0055 0.012
0.12 0.028 0.007⌐
0.14 0.032 0.008⌐
0.16 0.009⌐
0.18 ⌐0.171 0.036⌐0.0362 0.010⌐0.0097 ⌐0.0138
1.0 0.24 0.04 0.012⌐
0.32 0.05 0.014⌐
0.40 0.06
0.50 0.07
0.08 0.016⌐
0.5 0.60 ⌐0.575 0.09 ⌐0.063 0.018⌐0.0165 ⌐0.0126
0.70 0.12 0.024⌐
0.16 0.028⌐
0.80 ⌐0.802 0.20 0.032 0.014⌐
0.24 ⌐0.229 0.04 ⌐0.0363 0.016⌐0.0148
0.32 0.07 0.020
0.40 0.10 0.024
0.2 0.90 ⌐0.896 0.50 ⌐0.470 0.12 ⌐0.119 0.032⌐0.0287
0.20 0.10
0.60 0.24 0.16
0.28 0.20
0.32 0.24
0.36
0.1 0.951 0.70 ⌐0.711 0.335 0.273

16. 40. 70. 180.
ANGLE

MEAN RADIUS, MICRONS

Figure 8